Mineralium Deposita
https://doi.org/10.1007/s00126-018-0825-1

ARTICLE

Trace element composition of iron oxides from IOCG and IOA deposits: relationship to hydrothermal alteration and deposit subtypes

Xiao-Wen Huang[1,2,3] · Émilie Boutroy[2,4] · Sheida Makvandi[2,3] · Georges Beaudoin[2,3] · Louise Corriveau[5] · Anthony Franco De Toni[6]

Received: 12 January 2018 / Accepted: 3 July 2018

Abstract

Trace element compositions of magnetite and hematite from 16 well-studied iron oxide–copper–gold (IOCG) and iron oxide apatite (IOA) deposits, combined with partial least squares-discriminant analysis (PLS-DA), were used to investigate the factors controlling the iron oxide chemistry and the links between the chemical composition of iron oxides and hydrothermal processes, as divided by alteration types and IOCG and IOA deposit subtypes. Chemical compositions of iron oxides are controlled by oxygen fugacity, temperature, co-precipitating sulfides, and host rocks. Iron oxides from hematite IOCG deposits show relatively high Nb, Cu, Mo, W, and Sn contents, and can be discriminated from those from magnetite + hematite and magnetite IOA deposits. Magnetite IOCG deposits show a compositional diversity and overlap with the three other types, which may be due to the incremental development of high-temperature Ca–Fe and K–Fe alteration. Iron oxides from the high-temperature Ca–Fe alteration can be discriminated from those from high- and low-temperature K–Fe alteration by higher Mg and V contents. Iron oxides from low-temperature K–Fe alteration can be discriminated from those from high-temperature K–Fe alteration by higher Si, Ca, Zr, W, Nb, and Mo contents. Iron oxides from IOA deposits can be discriminated from those from IOCG deposits by higher Mg, Ti, V, Pb, and Sc contents. The composition of IOCG and IOA iron oxides can be discriminated from those from porphyry Cu, Ni–Cu, and volcanogenic massive sulfide deposits.

Keywords Trace elements · Iron oxides · Deposit subtypes · Alteration types · Discrimination diagram

Editorial handling: F. Melcher

Electronic supplementary material The online version of this article (https://doi.org/10.1007/s00126-018-0825-1) contains supplementary material, which is available to authorized users.

✉ Xiao-Wen Huang
huangxiaowen2008@live.cn

[1] State Key Laboratory of Ore Deposit Geochemistry, Institute of Geochemistry, Chinese Academy of Sciences, Guiyang 550081, China

[2] Département de Géologie et de Génie Géologique, Université Laval, Québec, QC G1V 0A6, Canada

[3] Research Center on the Geology and Engineering of Mineral Resources (E4m), Université Laval, Québec, QC G1V 0A6, Canada

[4] Agnico Eagle Mines Limited, 1655 3e Av, Val d'Or, QC J9P 1W1, Canada

[5] Geological Survey of Canada, Natural Resources Canada, 490 rue de la Couronne, Québec, QC G1K9A9, Canada

[6] SOQUEM Inc., 1740 chemin Sullivan, suite 2000, Val-d'Or, QC J9P 7H1, Canada

Introduction

The iron oxides, including magnetite and hematite, are common major or accessory minerals in igneous, sedimentary, and metamorphic rocks, and in various types of mineral deposits (Ramdohr 1980; Dupuis and Beaudoin 2011). A range of minor and trace elements such as Al, Ti, Mg, Mn, Zn, Cr, V, Ni, Co, and Ga can be incorporated into the inverse spinel structure of magnetite (Buddington and Lindsley 1964; Frost and Lindsley 1991; Dupuis and Beaudoin 2011; Nadoll et al. 2014). Trace elements in magnetite have been used as provenance indicators of sediments (Grigsby 1990; Razjigaeva and Naumova 1992; Makvandi et al. 2015), petrogenetic indicators (Barnes and Roeder 2001; Dare et al. 2014), and as mineral exploration tools (Dupuis and Beaudoin 2011; Boutroy et al. 2014; Sappin et al. 2014; Makvandi et al. 2015, 2016a, b). They are also widely used to fingerprint various deposit types or ore-forming processes (Müller et al. 2003; Carew 2004; Singoyi et al. 2006; Rusk et al. 2009;

Published online: 17 July 2018

Beaudoin and Dupuis 2010; Dupuis and Beaudoin 2011; Dare et al. 2012; Nadoll et al. 2012; Huang et al. 2013, 2015a, b, 2016; Chen et al. 2015; Knipping et al. 2015b; Liu et al. 2015).

The composition of magnetite and hematite is controlled by (1) the composition of magma (Dare et al. 2012, 2014; Liu et al., 2015), or composition of hydrothermal solutions which is determined by the composition of source rocks and fluid–rock interactions along the flow path (Carew 2004; Dare et al. 2012, 2014; Nadoll et al. 2014; Huang et al. 2016), (2) the physical and chemical conditions that influence the partition coefficients of elements, such as temperature, pressure, rate of cooling, oxygen fugacity, silica activity (Goldschmidt 1958; Buddington and Lindsley 1964; Fleet 1981; Wechsler et al. 1984; Whalen and Chappell 1988; Ghiorso and Sack 1991; Righter et al. 2006; Sievwright et al. 2017), and (3) the co-crystallization minerals during which some specific elements may compete with magnetite and hematite (Carew 2004; Dare et al. 2012; Huang et al. 2014; Nadoll et al. 2014).

The iron oxide–copper–gold (IOCG) deposit class has attracted growing exploration and research interest since the discovery of the giant Olympic Dam deposit (Hitzman et al. 1992). IOCG deposits are characterized by Cu-sulfides ± Au hydrothermal mineralization with abundant magnetite or hematite. They occur in rocks ranging in age from the Late Archean to the Mesozoic (Williams et al. 2005). These deposits show a great variation in geological settings, alteration systematics as well as mineralizing fluid compositions (Hitzman et al. 1992; Hitzman 2000; Sillitoe 2003; Williams et al. 2005). Iron oxide apatite (IOA) deposits are characterized by apatite-bearing iron ores lacking copper, gold and polymetallic mineralization beyond rare-earth elements (Williams 2010a). The IOA deposits studied are also referred to Kiruna-type IOA deposits that are characterized by Ti-poor magnetite. IOCG and IOA deposits can be subdivided into hematite, hematite + magnetite, and magnetite groups based on the principal iron oxide (Williams 2010a). Magnetite-group and hematite-group IOCG deposits form in a variety of hydrothermal environments, across distinct temperature ranges and fluid evolution processes (Skirrow 2010; Williams 2010b). Magnetite-group IOCG deposits represent the higher temperature part of the IOCG spectrum contrasting with hematite-group deposits, such as Olympic Dam, that are characterized by lower temperature hematite and white mica-dominated alteration (Williams 2010a). IOA deposits characterize a number of regions worldwide where they generally display an association with calc-alkaline arc magmatism (Barton and Johnson 1996; Williams et al. 2005). Both magnetite-group and magnetite + hematite-group IOA deposits are commonly enveloped by breccias with magnetite ± hematite ± actinolite matrix that occur within large scale Na ± Ca and high-temperature Ca–Fe alteration systems (Corriveau et al. 2010, 2016; Williams 2010a; Tornos et al. 2016).

Both IOCG and IOA deposits are closely associated with extensive hydrothermal alteration, divided into Na to Na–Ca alteration, high-temperature Ca–Fe, high-temperature K–Fe, and low-temperature K–Fe and Ca–Mg alteration types (Corriveau et al. 2010, 2016). Different alteration stages have characteristic mineral assemblages, chemical footprints and signatures, metal associations, formation temperature, and fluid composition (Corriveau et al. 2010, 2016; Montreuil et al. 2013, 2016).

Different classification schemes of iron oxides from IOCG and IOA deposits have been proposed based on trace element composition of iron oxides. Dupuis and Beaudoin (2011) have proposed the Ca + Al + Mn versus Ti + V and Ni/(Cr + Mn) versus Ti + V diagrams to discriminate IOCG and IOA deposits from Fe–Ti–V, porphyry, skarn deposits, and banded iron formation (BIF). In these diagrams, iron oxides from IOCG deposits can be separated from those from IOA deposits due to lower total Ti and V contents. Knipping et al. (2015b) used a plot of V vs. Cr to distinguish IOA deposits from magmatic Fe–Ti–V, porphyry, and IOCG deposits, on the basis that IOA deposits magnetite has lower Cr, but higher V, concentrations than IOCG deposits. Heidarian et al. (2016) and Broughm et al. (2017) demonstrated that the V versus Ti, V versus Ni + Co, V versus Ni, and V/Ti versus Ni/Ti diagrams, proposed by Loberg and Horndahl (1983), were useful to discriminate IOA deposits from magmatic Fe–Ti deposits and BIF. Despite the successful application of these diagrams, all of them have limitations with significant overlaps (e.g., Broughm et al. 2017). Binary score plots based on partial least squares-discriminant analysis (PLS-DA) proved to be efficient in separating IOCG and IOA deposits from porphyry, Ni–Cu, VMS deposits, and VMS-related BIF (Makvandi et al. 2016b). PLS-DA showed that magnetite from IOCG deposits is characterized higher Si, whereas magnetite from IOA deposits has higher Ti and Co concentrations (Makvandi et al. 2016b).

In this paper, we selected nine IOCG and seven IOA deposits representing major examples of both deposits, and their related alteration types (Fig. 1, Online Resource 1; Williams et al. 2005). These deposits formed in a range of geological environments with different ages, host rocks, and alteration assemblages, which are considered representative for both types of mineral deposits. By investigating the mineral paragenesis with emphasis on magnetite and/or hematite associated with mineralization, trace element composition of magnetite and hematite were determined by electron probe microanalyzer (EPMA) and laser ablation–inductively coupled plasma–mass spectrometry (LA-

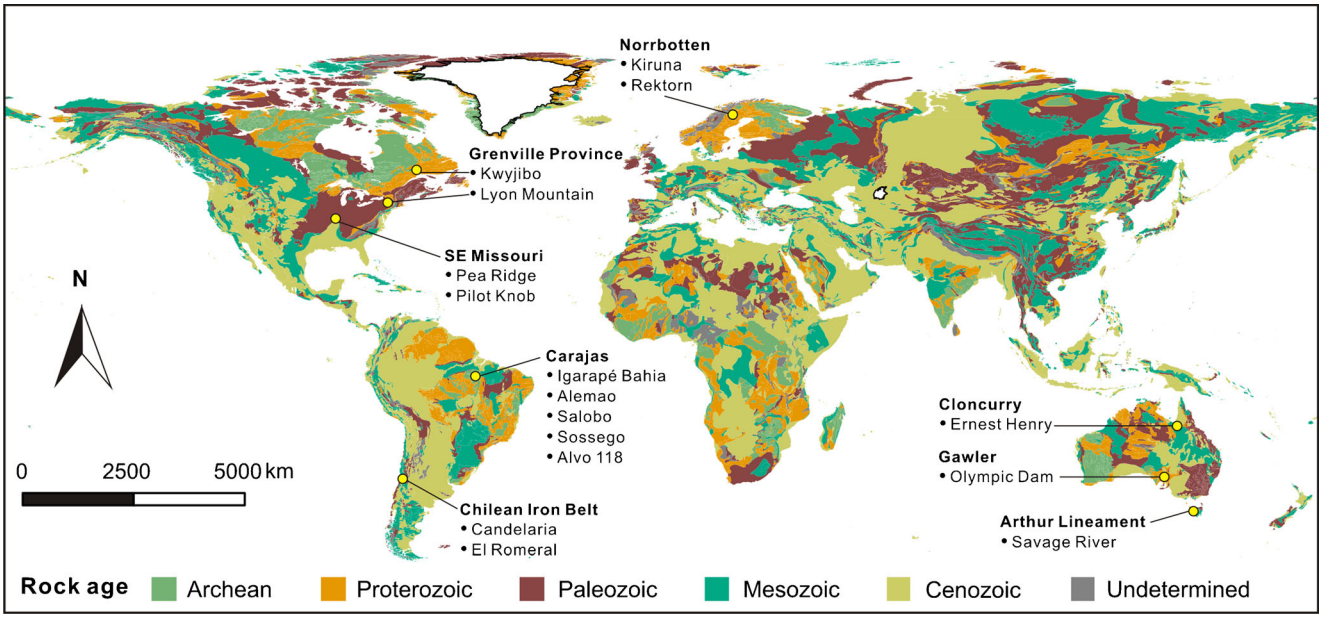

Fig. 1 Distribution of selected IOCG and IOA districts and related deposits. The physical map of world is from M. Colpron (Geological Survey of Canada)

ICP-MS). Based on these petrographic and geochemical analyses, we discuss the factors controlling the iron oxide chemistry and the links between the chemical composition of iron oxides and hydrothermal processes, as divided by alteration types and deposit subtypes.

Sample selection and classification

Sample selection

IOCG deposits include Igarapé Bahia, Alemao, Sossego, Alvo 118, and Salobo from the Carajas district in Brazil, Olympic Dam and Ernest Henry from the Gawler craton and the Cloncurry district, respectively, in Australia, Candelaria from the Central Andes district in Chile, and Kwyjibo from the Grenville Province in Canada (Fig. 1 and Online Resource 1). IOA deposits include Kiruna (or Kiirunavaara) and Rektorn from the Norrbotten district of northern Sweden, El Romeral from the Central Andes in Chile, Savage River from the Arthur Lineament in Australia, Pilot Knob and Pea Ridge from the Missouri district in the USA, and Lyon Mountain from the Grenville Province in USA (Fig. 1 and Online Resource 1). For each deposit studied, between one to ten polished sections or polished thin sections sampled from ore zones have been used, from which three to four magnetite and/or hematite grains have been analyzed by at least three spots per grain with the EPMA. The selected grains are in equilibrium with other mineral grains in order to avoid elemental exchange after their formation. Iron oxide grains with re-equilibration textures (Hu et al. 2015; Huang et al. 2018) are excluded because the chemical composition of these grains may have been modified during replacement. Selected larger grains were also analyzed by LA-ICP-MS.

Sample classification

Deposit subtypes

Williams (2010a) suggested that IOCG and IOA deposits can be subdivided into hematite, hematite + magnetite, and magnetite groups based on the nature of the principal iron oxides present. Each of these groups includes a number of different deposit subtypes that exhibit significantly different physical property distributions (e.g., density, remanence, conductivity, radiometric K and U). According to the type of major iron oxides, the deposits are divided into magnetite-group IOCG deposits, hematite-group IOCG deposit, magnetite-group IOA deposits, and magnetite + hematite-group IOA deposits (Online Resource 1).

Alteration types

Corriveau et al. (2010, 2016) proposed an alteration zoning model that frames the evolution of iron oxide and alkali-calcic hydrothermal systems and their iron oxide-apatite and magnetite- and hematite-group IOCG deposits. They defined five main alteration stages, reflecting declining temperature and increasing oxygen fugacity. The main alteration types are Na, high-temperature Ca–Fe, high-temperature K–Fe, low-temperature and hydrolytic K–Fe

as well as transitional Na–Ca–Fe, skarn, potassic felsite, potassic skarn, and low-temperature Ca–Mg alteration.

Early Na (± Ca) and high-temperature Ca–Fe (± Na) alteration zones are commonly laterally extensive, regional in scale and commonly lack polymetallic mineralization unless replaced by fertile K–Fe alteration types. Sodic alteration principally results in albitite, which generally contains variable amounts of scapolite and cryptocrystalline quartz (Corriveau et al. 2016). The Ca–Fe alteration consists of variable proportions of amphibole (actinolite or hornblende) and magnetite as well as accessory apatite, garnet, and clinopyroxene. With garnet and clinopyroxene, epidote is commonly part of earlier skarn assemblages formed after, or coeval, with albitization and subsequently incrementally replaced by amphibole during high-temperature Ca–Fe alteration. The high-temperature K–Fe alteration consists of variable proportions of K-feldspar, magnetite, and biotite, whereas the low-temperature K–Fe alteration consists of hematite, chlorite, K-feldspar, white mica (sericite), carbonates, and quartz. All the samples were classified according to the alteration type that hosts the IOCG or IOA mineralization based on the mineral assemblages observed in thin sections and alteration description in literature (Online Resource 2).

Methodology

Analytical methods

EPMA analyses

Major and minor/trace elements in iron oxides were analyzed at Université Laval using a CAMECA SX-100 EPMA, equipped with five wavelength-dispersive spectrometers, using a 10-μm-diameter beam with a voltage of 15 kV and a current of 100 nA. Minor and trace elements K, Ca, Al, Si, Ti, Mg, Mn, Cr, V, Sn, Cu, Zn, and Ni typically have element concentrations commonly above the detection limit. Analytical conditions are similar to those described by Boutroy et al. (2014). Calibration was achieved using a range of natural and synthetic standards, comprising simple oxides (GEO Standard Block of P and H Developments) and natural minerals (Mineral Standard Mount MINM 25–53, Astimex Scientific) (Jarosewich et al. 1980). The background was measured on one side of the peak for 15–20 s at a position free of interfering element X-ray and the concentration was counted over the peak for 20 to 40 s depending on the element. Detection limits are ~ 100 ppm for Zn; ~ 80 ppm for Cu; ~ 60 ppm for Ni; 40–50 ppm for V, Cr, Mn, and Sn; and 15–25 ppm for K, Ca, Ti, Al, Si, and Mg (Online Resource 3).

LA-ICP-MS analyses

Iron oxides were analyzed by using a RESOlution M-50193 nm Excimer Laser Ablation system coupled with an Agilent 7700× ICP-MS at Université du Québec à Chicoutimi (UQAC), using a beam size of 25 to 80 μm with a speed stage of 3 to 15 μm/s and a laser frequency of 10 Hz and a power of 5 mJ per pulse. The minor and trace elements ^{24}Mg, ^{27}Al, ^{45}Sc, ^{47}Ti, ^{51}V, ^{52}Cr, ^{55}Mn, ^{60}Ni, ^{66}Zn, ^{75}As, ^{59}Co, $^{69, 71}$Ga, ^{74}Ge, ^{89}Y, $^{90, 92}$Zr, ^{95}Mo, ^{101}Ru, ^{105}Pd, ^{111}Cd, ^{118}Sn, ^{121}Sb, ^{93}Nb, ^{107}Ag, ^{115}In, ^{178}Hf, ^{181}Ta, ^{182}W, ^{187}Re, ^{193}Ir, ^{195}Pt, ^{197}Au, ^{208}Pb, and ^{209}Bi were measured. Sulfur, Si, Ca, and Cu were monitored to detect mineral inclusions. Multiple isotopes of Zr and Ga were measured to resolve isobaric interferences. Analytical conditions are similar to those described by Boutroy et al. (2014). A single Fe-rich reference material, GSE-1G containing all the required elements, was used for calibration (Savard et al. 2012). To monitor the quality of the analyses, reference materials GSD-1G and BC28 (natural magmatic magnetite) were routinely analyzed. Data reduction was carried out using the software Iolite. Lines were ablated across the width of a magnetite grain for a period ranging from 20 to 60 s depending on the grain size, after monitoring a gas blank for 20–30 s. Iron was used as the internal standard to compute concentration assuming stoichiometric magnetite (Dare et al. 2012). Detection limits are 0.01 to 0.02 ppm for ^{24}Mg, ^{59}Co, ^{89}Y, $^{90.92}$ Zr, ^{93}Nb, ^{101}Ru, ^{105}Pd, ^{107}Ag, ^{115}In, ^{181}Ta, ^{182}W, ^{187}Re, ^{197}Au, ^{208}Pb, and ^{209}Bi; 0.025 to 0.05 ppm for ^{45}Sc, ^{51}V, ^{95}Mo, and ^{178}Hf; 0.055 to 0.1 ppm for ^{65}Cu, ^{71}Ga, ^{111}Cd, ^{121}Sb, ^{193}Ir, and ^{195}Pt; 0.1 to 0.5 ppm for ^{27}Al, ^{47}Ti, ^{60}Ni, ^{66}Zn, ^{74}Ge, ^{75}As, ^{118}Sn; and 0.55 to 1 ppm for ^{52}Cr and ^{55}Mn (Online Resource 4).

Statistical methods

Estimation of average composition

Electron microprobe and LA-ICP-MS datasets are typically censored because they contain non-detects that are below the computed minimum detection limits (Helsel 2005). The average composition of iron oxides is estimated using the nonparametric Kaplan-Meier (K-M) method (NADA package in R; Lee and Helsel 2007).

Data preprocessing and partial least squares-discriminant analysis

In order to investigate the possible factors controlling the variations of trace element composition of iron oxides and unravel the relationships between iron oxide chemistry and host rocks, alteration and deposit types, the individual

EPMA and LA-ICP-MS analyses were investigated by partial least squares-discriminant analysis (PLS-DA). PLS-DA can also identify discriminant elements separating different sample classes based on iron oxide compositions. Seven of thirteen elements analyzed by EPMA are investigated by PLS-DA, whereas K, Sn, Cu, Zn, Ni, and Cr were excluded because the dataset contains more than 40% censored data. According to this criterion, Y, P, Ta, and Hf, analyzed by LA-ICP-MS, are not considered for PLS-DA.

Censored compositional data were imputed using the k-nearest neighbors function with the Aitchison distance (robCompositions package in R; Hron et al. 2010; Makvandi et al. 2016b). Geochemical data, summed to 100%, can lead to spurious correlations when studying co-variations (Aitchison 1986; Whitten 1995). This is referred as the "closure problem," inherent to all compositional datasets (Aitchison 1986). In this study, data were transformed using centered-log ratio (clr) method (Thió-Henestrosa and Martín-Fernández 2005) that is a suitable method for multivariate statistical techniques such as PLS-DA (Aitchison 1986; Egozcue et al. 2003; Makvandi et al. 2016b).

Statistical analysis was carried out using PLS-DA method as described in Makvandi et al. (2016b). PLS-DA is a supervised classification technique using labeled data, which sharpens the separation between groups of observations by rotating principal components, and results in the maximum separation among classes and the identification of the variables responsible for the separation of different classes (De Iorio et al. 2008). In the PLS-DA method, a series of orthogonal components (latent variables) are extracted to relate the X (N × K) and Y (N × M) matrices by maximizing the covariance between the two matrices using the following equations (Wold et al. 2001; Eriksson et al., 2013; Brereton and Lloyd 2014):

$$X = TP^{T} + E \quad (1)$$

$$Y = TQ^{T} + F \quad (2)$$

$$T = XW^{*} \quad (3)$$

where T (N × r) is the score matrix containing r orthogonal PLS components (scores). The T matrix represents the common latent variable space of both X and Y matrices. For Eqs. (1)–(3), P (N × r) and Q (M × r) are the loadings matrices for X and Y, respectively. The weight matrix (W*) consists of the coefficients of the linear combinations of the X variables that are the most predictive of Y, whereas E and F are the model residuals.

Following Makvandi et al. (2016b), loadings and weights biplots (qw^*_1–qw^*_2), score scatter plots (t_1–t_2), score contribution plots, and variable importance on projection (VIP) plots were generated for different datasets. Loadings biplots indicate the correlation among different variables (elements), and the relationship between the variables and different sample classes (e.g., host rock/deposit type/alteration type). The loading values show the impact of elements on the model, and the sign of the values indicates the positive or negative correlation between the elements. As a result, elements that plot in the vicinity of each other in the PLS-DA loadings space show strong positive correlations, and they are negatively correlated to those in an opposite quadrant. The correlation among variables and sample classes control the distribution of samples in the score scatter plots. Score contribution plots depict the compositional differences between the mean composition of a cluster (sample group) and the mean composition of the whole dataset. Given that data is mean-centered prior to PLS-DA, the origin of score scatter plots represents the mean composition of the whole dataset (Makvandi et al. 2016b). The VIP plots are also used to indicate the impact of different variables on the sample classification, where VIP values equal and/or larger than 1 are the most important in the classification (Eriksson et al. 2013).

Results

Petrography of mineralization and alteration

The mineral assemblages of each thin section are characterized by macroscopic and microscopic observation (Online Resource 2). Combined with the description of hydrothermal alteration in each deposit, the mineral assemblages in thin section are used to define deposit subtypes and alteration types.

Igarapé Bahia The main iron oxide in the Igarapé Bahia Cu–Au deposit is magnetite (Fig. 2a), and thus this deposit is classified into magnetite-group IOCG deposits. The hydrothermal alteration and mineralization at this deposit is characterized by (1) Fe metasomatism leading to the formation of grunerite, fayalite, and/or Fe oxides (magnetite and/or hematite), (2) carbonate alteration (mainly siderite), (3) chalcopyrite and bornite, (4) quartz-poor gangue, (5) low REE, and (6) enrichment in U and Co from early to late (Tazava and De Oliveira 2000; Tallarico et al. 2005; Dreher et al. 2008). Three samples from this deposit have similar mineral assemblages of magnetite, chalcopyrite, and siderite (Fig. 2a), which is typical of Fe metasomatism. Magnetite is subhedral to euhedral with grain size from a few microns to ~300 μm (Fig. 2a). The primary Cu–Au mineralization in Igarapé Bahia is closely related to Fe chlorite, siderite, and magnetite-rich breccias (Tallarico et al. 2005). Magnetite breccias exhibit a granular matrix of euhedral magnetite cemented by chalcopyrite and bornite,

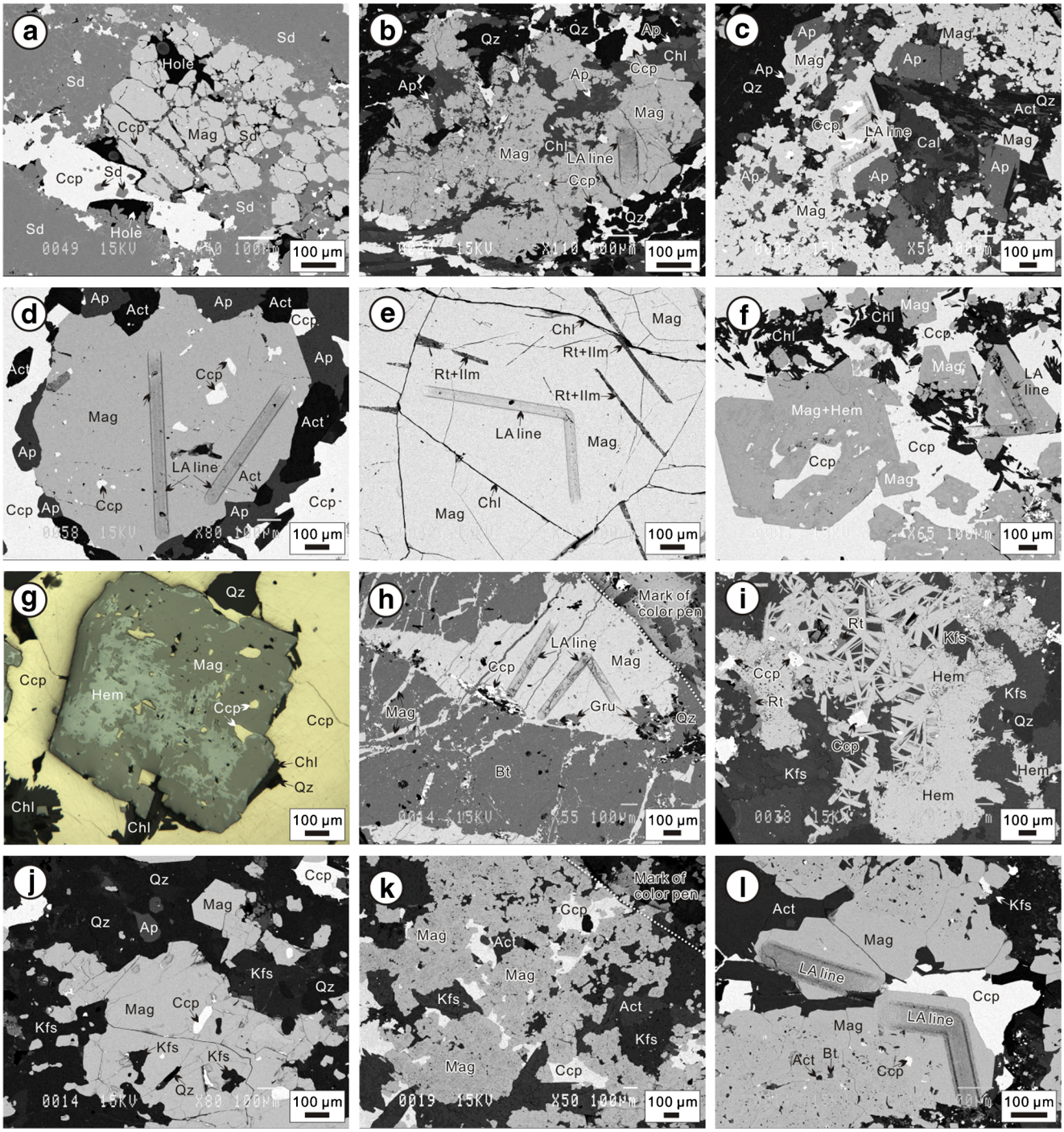

Fig. 2 Photomicrographs of ores from the IOCG deposits. All images are acquired by back-scattered electron (BSE) imaging except one in (**g**) by reflected light. **a** Ore from the Igarapé Bahia deposit (F332A) where magnetite and chalcopyrite are brecciated and cemented by siderite. **b** Ore from the Alemao deposit (Alemao) consisting of subhedral magnetite and accessory apatite replaced by quartz, chlorite, and minor chalcopyrite. **c** Ore from the Sossego deposit (080) composed of euhedral to subhedral magnetite and apatite and minor chalcopyrite cut by a quartz and calcite assemblage. **d** Ore from the Sossego deposit (F259) composed of subhedral magnetite, apatite, actinolite, and chalcopyrite. **e** Magnetite grains from the Sossego deposit (SOS_39K) with exsolution lamellae of rutile and ilmenite. Fractures of magnetite are filled by chlorite. **f** Ore from the Alvo 118 deposit (AF443) composed of euhedral to subhedral magnetite and chalcopyrite replaced by chlorite. **g** Part of magnetite from the sample AF443 of the Alvo 118 deposit was transformed to hematite. **h** Ore from the Salobo deposit (F159) composed of magnetite, biotite, and minor grunerite and chalcopyrite. **i** Ore from the Olympic Dam (OD3) consisting of hematite, K-feldspar, quartz, and minor chalcopyrite and rutile. **j** Ore from the Ernest Henry deposit (EH1) composed of magnetite, K-feldspar, apatite, quartz, and chalcopyrite. **k** Ore from the Candelaria deposit (LD367B) composed of magnetite, K-feldspar, actinolite, and chalcopyrite. **l** Euhedral magnetite in ore from the Candelaria deposit (Candelaria) was filled by actinolite, biotite, and chalcopyrite. *Ab* albite, *Act* actinolite, *Ap* apatite, *Bt* biotite, *Cal* calcite, *Ccp* chalcopyrite, *Chl* chlorite, *Ep* epidotite, *Gru* grunerite, *Hem* hematite, *Ilm* ilmenite, *Kfs* K-feldspar, *Rt* rutile, *Sd* siderite, *Ttn* titanite, *Mag* magnetite, *Qz* quartz

together with minor grunerite, actinolite, minnesotaite, biotite, stilpnomelane, K-feldspar, tourmaline, fluorite, siderite, ankerite, and uraninite (Tallarico et al. 2005). This mineral assemblage defines a distinctive K–Fe-enriched zone in the deposit (Tallarico et al. 2005), belonging to the high-temperature K–Fe alteration facies.

Alemao The main iron oxide in the Alemao Cu–Au deposit is magnetite (Fig. 2b), which defines this deposit as a magnetite-group IOCG deposit. The hydrothermal alteration at Alemao includes (1) Fe metasomatism leading to the formation of grunerite, fayalite, and/or Fe oxides (magnetite and/or hematite), (2) intense chloritization (Mg and Fe chlorite), (3) biotitization, (4) chalcopyrite and bornite, (5) intense carbonate alteration (mainly siderite), and (6) local silicification and tourmalinization from early to late (Barreira et al. 1999; Ronzê et al. 2000). One sample contains subhedral magnetite and accessory apatite replaced by an assemblage of quartz and chlorite (Fig. 2b). Magnetite is interpreted to form part of the high-temperature Ca–Fe alteration facies.

Sossego The iron oxides in the Sossego Cu–Au deposit include magnetite and ilmenite (Fig. 2c–e), and thus this deposit is classified as a magnetite-group IOCG deposit. It consists of two major groups of orebodies, Sequeirinho–Pista–Baiano (SPB) and Sossego–Curral (SC), with distinct types of hydrothermal alteration. The SPB orebodies have undergone regional sodic alteration (albite) and later actinolite-rich high-temperature Ca–Fe alteration associated with the formation of massive magnetite–(apatite) bodies (Monteiro et al. 2008a, b; Xavier et al. 2012). Spatially restricted zones of high-temperature K–Fe (biotite and K-feldspar) alteration overprint the Ca–Fe assemblage and grade outward to chlorite-rich zones. Within the SC orebodies, early albitic and subsequent high-temperature Ca–Fe alteration are poorly developed, whereas the high-temperature K–Fe alteration assemblages mark the onset of the mineralization and grade outward to a widespread zone of chlorite and late hydrolytic low-temperature K–Fe (sericite–hematite–quartz) alteration crosscut by calcite veins (Monteiro et al. 2008a, b; Xavier et al. 2012). Three samples, 080, 081, and 084, are from the SC orebodies, and the other three samples, F263P, F259, and SOS_39K, are from the SPB orebodies. Samples from the SC orebodies have a similar mineral assemblage of magnetite, apatite, actinolite, quartz, calcite, and chalcopyrite (Fig. 2c). Magnetite is anhedral to subhedral and is associated with apatite and chalcopyrite. Samples from the SPB orebodies are composed of magnetite, apatite, actinolite, and chalcopyrite (Fig. 2d). Some magnetite grains have exsolution lamellae of rutile and ilmenite (Fig. 2e). All samples from the Sossego deposit are grouped into the high-temperature Ca–Fe alteration type.

Alvo 118 The iron oxides in the Alvo 118 Cu–Au deposit include magnetite and minor hematite (Fig. 2f, g), which classifies this deposit as a magnetite-group IOCG deposit. It is hosted by mafic to felsic metavolcanic rocks and crosscutting granitoid and gabbro intrusions. Several hydrothermal alteration zones formed toward the ore zones: (1) poorly developed Na alteration (albite and scapolite); (2) high-temperature K–Fe alteration (biotite or K-feldspar) accompanied by magnetite and silicification; (3) widespread, pervasive chlorite alteration spatially associated with quartz–carbonate–sulfide cemented breccia and vein stockworks (low-temperature Ca-Mg); and (4) local post-ore quartz–sericite alteration (Torresi et al. 2012; Xavier et al. 2012). One sample (AF443) from the Alvo 118 deposit is composed of magnetite, hematite, chalcopyrite, chlorite, and quartz (Fig. 2f, g). Magnetite is subhedral to euhedral and associated with chalcopyrite. Chlorite and quartz are interstitial to magnetite and chalcopyrite (Fig. 2g). Because magnetite formation was closely related to potassic minerals (Torresi et al. 2012), the sample from this deposit is classified into high-temperature K–Fe alteration type.

Salobo The Salobo Cu–Au–Ag deposit is defined as a magnetite-group IOCG deposit (Fig. 2h). The ore-bearing, magnetite-rich rocks are the product of strong Fe–K alteration at high temperatures (550–650 °C) and have been deformed and mylonitized (Lindenmayer and Teixeira 1999; Requia and Fontboté 2000; Requia et al. 2003). The Fe–K alteration is replaced by widespread chlorite alteration (< 370 °C) accompanied by the formation of calcite, epidote, albite, sericite, quartz, and fluorite (Xavier et al. 2012). In the magnetite-rich rocks, chlorite replaces the Fe–Mg silicates (almandine, biotite, and hastingsite) and was followed by formation of greenalite around fayalite and grunerite associated with fluorite and uraninite (Lindenmayer and Teixeira 1999; Requia and Fontboté 2000; Xavier et al. 2012). Four samples from this deposit are composed of magnetite, biotite, and minor grunerite and chalcopyrite (Fig. 2h), which are attributed to the high-temperature K–Fe alteration. Magnetite occurs as massive aggregates associated with biotite. Chalcopyrite is disseminated in biotite or grows along the margin of magnetite (Fig. 2h).

Olympic Dam The main iron oxide in the Olympic Dam Cu–U–Au–Ag deposit is hematite (Fig. 2i), the archetype of hematite-group IOCG deposit (Williams 2010a). The key hydrothermal alteration assemblages are magnetite–pyrite–fluorapatite, and hematite–sericite–K-feldspar–chlorite–carbonate ± Fe–Cu sulfides ± U and REE minerals (Bastrakov et al. 2007; Apukhtina et al. 2017; Kontonikas-Charos et al. 2017). These two alteration assemblages reflect the transition

from early, high-temperature, and reduced fluids, followed by late, low-temperature, oxidized fluids, and from sulfide to sulfate-dominated conditions of low-temperature K–Fe alteration (Ehrig et al. 2012, 2017). Ten samples from this deposit are composed of hematite, K-feldspar, quartz, and minor chalcopyrite and rutile (Fig. 2i).

Ernest Henry The Ernest Henry Cu–Au deposit is a typical magnetite-group IOCG deposit (Fig. 2j; Williams 2010a). Hydrothermal alteration and mineralization is characterized by a regional pre-ore Na and Na–Ca alteration, overprinted by a pre-ore K–Fe–(Mn–Ba)-rich alteration that is represented by intense biotite–magnetite and magnetite–K-feldspar assemblage, and less common K-feldspar–garnet (manganese-rich) alteration (Mark et al. 2006; Corriveau et al. 2010; Rusk et al. 2010). K-feldspar alteration is most intense in the vicinity of copper–gold mineralization, and forms a halo extending from several hundred meters up to 2 km beyond the ore body (Mark et al. 2006). Four samples from this deposit have a similar mineral assemblage of magnetite, K-feldspar, and minor apatite, quartz, and chalcopyrite (Fig. 2j), which belong to the high-temperature K–Fe alteration.

Candelaria The main iron oxide in the Candelaria Cu–Au–Ag deposit is magnetite (Fig. 2k, l; Williams 2010a). Alkali metasomatism is widespread in Candelaria, including sodic (albite and/or marialitic scapolite) or K–Fe (biotite and/or K-feldspar) alteration related to ore formation (Marschik and Fontboté 2001; Marschik et al. 2003). The Cu–Fe (chalcopyrite + magnetite ± hematite) ores are associated with biotite–potassium feldspar ± calcic amphibole ± epidote alteration at Candelaria (Marschik and Fontboté 2001). Ten samples were chosen in this deposit, which have a mineral assemblage of magnetite, K-feldspar, actinolite, biotite, and chalcopyrite (Fig. 2k, l) of the high-temperature K–Fe alteration type. Magnetite is subhedral to euhedral and commonly contains inclusions of actinolite, biotite, and chalcopyrite (Fig. 2l).

Kwyjibo The iron oxide in the Kwyjibo Cu–REE–Mo–F–U–Au deposit is mainly magnetite (Fig. 3a, b). The hydrothermal alteration at Kwyjibo is characterized by widespread Ca–Fe alteration and locally important high-temperature K–Fe and Na–Ca alteration, hematitization, silicification, and late sodic alteration (Gauthier et al. 2004; Clark et al. 2005, 2010; Corriveau et al. 2007). Early Ca–Fe and K–Fe alteration with Na depletion results in vein magnetite–titanite mineralization. Late sodic alteration is local and associated with sulfides. Hematite crystallized relatively early, during shearing, and also at a late stage as an alteration product of magnetite. Peripherally to the magnetite-rich deposits at Kwyjibo, base metal sulfides were deposited in association with a strong calcic–silicate alteration. Three samples from this deposit have a mineral assemblage of magnetite, K-feldspar, biotite, quartz, and minor titanite (Fig. 3a, b), which belong to the high-temperature K–Fe alteration.

Kiruna The main iron oxide in the Kiruna Fe deposit is magnetite (Fig. 3c), and therefore this deposit is a magnetite-group IOA deposit. Host rock alteration around Fe orebodies is characterized by actinolite and biotite of the high-temperature Ca–Fe alteration type (Carlon 2000). The sample from the Kiruna deposit consists of magnetite, apatite, actinolite, and minor chlorite and biotite (Fig. 3c). Magnetite is subhedral to euhedral and has grain size ranging from ~ 100 to 1000 μm.

Rektorn The iron oxides in the Rektorn Fe deposit include magnetite and hematite (Fig. 3d, e), and therefore this deposit is classified as magnetite + hematite-group IOA deposit. The Rektorn Porphyry in the lowest part of hanging wall rocks is strongly altered rhyolite that varies from a massive K-feldspar to a strongly silicified rock containing spherulitic aggregates of K-feldspar and disseminated hematite (Geijer 1910; Martinsson et al. 2016). Sericite commonly occurs as a late-stage pervasive alteration in shear zones, but also occurs as patches or lenses of massive sericite containing radiating aggregates of tourmaline. The sample from the Rektorn deposit is composed of magnetite, hematite, apatite, and minor K-feldspar and monazite and belongs to high-temperature Ca–Fe alteration (Fig. 3d, e). Magnetite is anhedral and was partly or nearly wholly transformed to hematite (Fig. 3d).

El Romeral The main iron oxide in El Romeral is magnetite (Fig. 3f), and therefore this Fe deposit is classified as magnetite-group IOA deposit. The hydrothermal alteration in this deposit is represented by actinolitization, chloritization, argillization, and martitization (Bookstrom 1977). Magnetite deposition was accompanied by pervasive actinolitization, followed by chloritization and alteration of previously actinolitized diorite and phyllite. Altered rocks within and around the orebodies contain magnetite, actinolite, plagioclase, diopside, clinozoisite, titanite, chlorapatite, marialitic scapolite, tourmaline, chlorite, pyrite, calcite, mica, and clays (Bookstrom 1977). The sample from the El Romeral deposit consists of magnetite, actinolite, and minor albite (Fig. 3f), which indicates high-temperature Ca–Fe alteration.

Savage River The Savage River is a magnetite-group IOA deposit (Fig. 3g). This deposit consists of several lenses of magnetite-rich ore with amphibole (dominantly tremolite–actinolite), serpentine, talc, dolomite, calcite, pyrite, chlorite, albite, quartz, apatite, and hematite (Green 2012). The sample

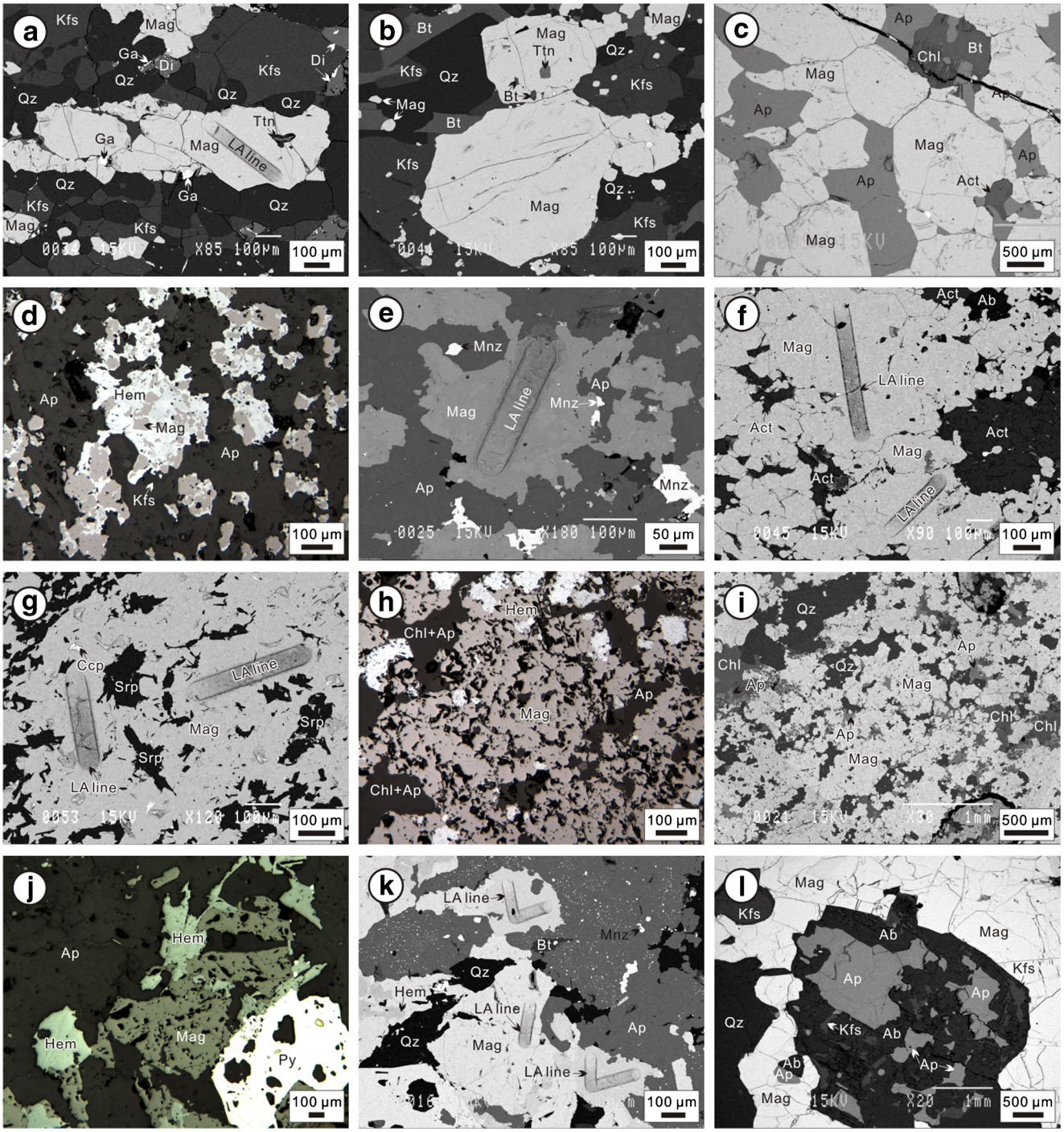

Fig. 3 Photomicrographs of ores from the IOA deposits except (**a**) and (**b**) from IOCG deposits. (**d**), (**h**), and (**j**) are under reflected light, whereas others are BSE images. **a** Ore from the Kwyjibo deposit (KJ3) composed of subhedral to euhedral magnetite, K-feldspar, diopside, and quartz. Minor titanite and galena replaced magnetite. **b** Ore from the Kwyjibo deposit (KJ1) consisting of euhedral magnetite, K-feldspar, biotite, quartz, and minor titanite. **c** Ore from the Kiruna deposit (Kiruna 1154) consisting of magnetite, apatite, actinolite, and minor chlorite and biotite. **d** Ore from the Rektorn deposit (1053) composed of magnetite, hematite, apatite, and minor K-feldspar. Magnetite was partly replaced by hematite. **e** Ore from the Rektorn deposit (1053) composed of magnetite, apatite, and monazite. **f** Ore the El Romeral deposit (El Romeral) consisting of magnetite, albite, and actinolite. **g** Ore from the Savage River deposit (Sriver) composed of magnetite, serpentine, and chalcopyrite. **h** Ore from the Pilot Knob deposit (1158) composed of magnetite and hematite. **i** Ore from the Pilot Knob deposit (1158) composed of magnetite, apatite, chlorite, and quartz. **j** Ore from the Pea Ridge deposit (1157) consisting of magnetite, hematite, and minor pyrite. **k** Ore from the Pea Ridge deposit (1157) consisting of magnetite, quartz, apatite, and minor biotite and monazite. **l** Ore from the Lyon Mountain deposit (99-4A) are composed of magnetite, albite, apatite, and minor K-feldspar. *Ab* albite, *Act* actinolite, *Ap* apatite, *Bt* biotite, *Ccp* chalcopyrite, *Di* diopside, *Chl* chlorite, *Ga* galena, *Hem* hematite, *Kfs* K-feldspar, *Mnz* monazite, *Srp* serpentine, *Ttn* titanite, *Mag* magnetite, *Qz* quartz

from the Savage River deposit is mainly composed of magnetite and serpentine (Fig. 3g). Minor chalcopyrite is disseminated in magnetite. The sample is ascribed to high-temperature Ca–Fe alteration based on the abundance of amphibole (Green 2012).

Pilot Knob The iron oxides in the Pilot Knob Fe deposit include magnetite and hematite (Fig. 3h, i), and thus this deposit is defined as magnetite + hematite-group IOA deposit. Wall rock alteration is rare at Pilot Knob, where minor sericite replaces albite and K-feldspar. Late-stage hydrothermal quartz veins containing chlorite and epidote, and orthoclase veins cut the ore (Nold et al. 2013). The dominant gangue minerals are albitic plagioclase, K-feldspar, quartz, and chlorite. The sample is composed of magnetite, hematite, apatite, chlorite, and quartz (Fig. 3h, i), which belongs to the high-temperature Ca–Fe alteration.

Pea Ridge The iron oxides in the Pea Ridge Fe deposit are mainly magnetite and hematite (Fig. 3j, k), and thus this deposit is classified as magnetite + hematite-group IOA deposit. Alteration at Pea Ridge includes silicification, potassic metasomatism, and alteration of the host rocks to actinolite, chlorite, epidote, and garnet (Nuelle et al. 1992; Day et al. 2016). The amphibole–quartz zone represents the earliest phase of alteration related to ore formation. Specular hematite is partly the result of replacement of magnetite. During and after the development of specularite, a massive silicified zone forms by filling empty spaces and the replacement of the host rock. The K–Fe (K-feldspar and magnetite) alteration and sericitization (sericite and hematite) accompany silicification. The sample from the Pea Ridge deposit consists of magnetite, hematite, apatite, quartz, minor pyrite, biotite, and monazite and belongs to the high-temperature Ca–Fe alteration (Fig. 3j, k).

Lyon Mountain The main iron oxides in the Lyon Mountain deposit are magnetite and hematite (Fig. 3l) and thus belongs to the magnetite + hematite-group IOA deposit type. The main Fe mineralization is characterized by "skarn-like" clinopyroxene-magnetite ± apatite assemblages associated with migmatization and mylonitization and occasionally potassic alteration (McLelland et al. 2002; Valley et al. 2010). Two samples from Lyon Mountain are composed of magnetite, albite, apatite, and minor K-feldspar and quartz (Fig. 3l), which belong to the high-temperature Ca–Fe alteration.

Average trace element composition of iron oxides

A total of 521 spot analyses by EPMA and 124 line analyses by LA-ICP-MS were obtained on 50 sections (Online Resource 2). Full analytical results of EPMA and LA-ICP-MS are shown in Online Resources 3 and 4. Figures in Online Resources 5 and 6 display the chemical composition of individual analyses and average composition of each sample, normalized to bulk continental crust, whereas Fig. 4 provides the average composition of individual deposits, normalized to bulk continental crust. EPMA data show that samples from the same deposit have similar normalized trace element patterns and that normalized ratios of a specific element vary within one order of magnitude (Online Resource 5). Magnetite and hematite from the same deposit have similar trace element patterns (Online Resource 5). LA-ICP-MS data show that samples from the same deposit have more variable trace element compositions with normalized Pb, Zr, Mo, and Sn contents variation exceeding one order of magnitude (Online Resource 6). For IOCG deposits, samples from the Alvo 118 deposit have lower Mg and Ti contents, whereas those from the Sossego deposit have higher V and Ni contents (Fig. 4a, c). For IOA deposits, samples from the Kiruna deposit have lower Ti content, whereas those from the Lyon Mountain have lower V content (Fig. 4b, d). LA-ICP-MS data show that samples from different IOCG deposits have Y, P, Pb, Zr, W, Ta, Nb, Mo, Sn, V, Ni, and Cr contents varying between one and three orders of magnitude (Fig. 4c), whereas samples from different IOA deposits have Ca, Y, Pb, Zr, W, Sc, Ta, Nb, Sn, Mg, and Co contents varying from one to four orders of magnitude (Fig. 4d). Samples from the Pea Ridge deposit show W and Sn enrichment relative to other IOA deposits (Fig. 4d).

Average trace element compositions of each deposit are plotted in Ca + Al + Mn versus Ti + V and Ni/(Cr + Mn) versus Ti + V diagrams proposed by Dupuis and Beaudoin (2011). In general, LA-ICP-MS data have lower Ni/(Cr + Mn) ratios than EPMA data, which is mainly due to lower detection limit for Ni and Cr (Fig. 5a). LA-ICP-MS data have slightly higher Ca + Al + Mn values than EPMA data (Fig. 5b), which may be due to some undetected mineral inclusions during LA-ICP-MS analysis. Most deposits have LA-ICP-MS Ti + V contents slightly higher than EPMA Ti + V contents, with the exception of Olympic Dam and Salobo deposits (Fig. 5a, b). The slightly higher EPMA Ti + V contents than LA-ICP-MS Ti + V contents in Salobo magnetite may be due to higher EPMA detection limits of these elements, whereas the higher EPMA Ti + V contents (~ 0.23 wt.%) than LA-ICP-MS Ti + V contents (~ 0.08 wt%) in Olympic Dam hematite are due to microscopic Ti-rich mineral inclusions in sample OD2 that was analyzed by EPMA but not by LA-ICP-MS. This likely explains why LA-ICP-MS data from Olympic Dam plot in the IOCG field, whereas EPMA data of this deposit plot between the Kiruna and Porphyry fields (Fig. 5a, b). As shown in Fig. 5a, three IOCG deposits plot in the IOCG field and four IOA deposits in the Kiruna field. Both EPMA and LA-ICP-MS data of Sossego plot above the Kiruna field, whereas those of Kiruna, Pea Ridge, and El Romeral plot in the Porphyry field

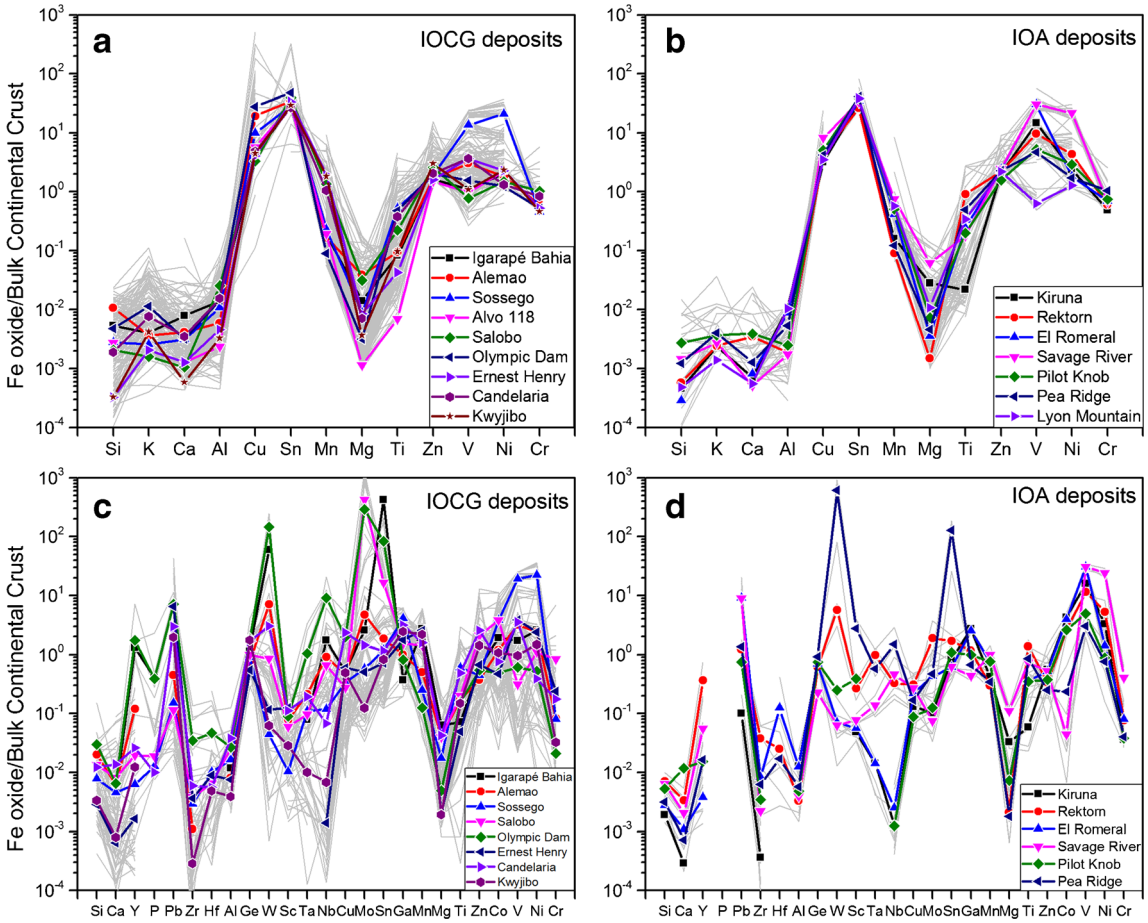

Fig. 4 Multi-element diagrams of average trace element composition of iron oxides from individual deposits, normalized to bulk continental crust (Rudnick and Gao 2003). The light gray lines represent individual analyses. **a**, **b** EPMA data of IOCG and IOA deposits. **c**, **d** LA-ICP-MS data of IOCG and IOA deposits

(Fig. 5a). However, in the Ca + Al + Mn versus Ti + V diagram (Fig. 5b), most IOCG and IOA deposits plot in the IOCG and Kiruna fields, respectively, indicating that this diagram is more reliable. The exceptions are Candelaria, which plots at the Porphyry field, and Sossego, which plots at the boundary between Porphyry and Kiruna fields.

Chemical composition of iron oxides from different deposit and alteration types

The minimum, maximum, median, and average trace element contents of iron oxides from different deposit and alteration types are shown in Fig. 6. EPMA analyses show that iron oxides from different subtypes of IOCG and IOA deposits have different trace element concentrations. Iron oxides from the hematite-group IOCG deposits have relatively high Si, Ca, Al, Sn, Cu, and Ti contents but low Mn, Mg, V, and Ni contents, whereas those from the magnetite-group IOCG deposits are characterized by relatively high Mn contents (Fig. 6a). Iron oxides from the magnetite-group IOA deposits have relatively high Mg, Zn, V, and Ni contents and low Si, K, Ca, and Ti contents, whereas those from the magnetite + hematite-group IOA deposits are characterized by relatively high Ti but low Al contents (Fig. 6a). LA-ICP-MS analyses show that magnetite-group IOCG deposits are characterized by relatively low Pb, Zr, and Sc and high Ga, Mn, Zn, Ni, and Cr, whereas those from the hematite-group IOCG deposits are characterized by high Si, Ca, Pb, Zr, W, Sn, Nb, Cu, and Mo but low Ga, Mn, Mg, Ti, Co, V, Ni, and Cr (Fig. 6b). Iron oxides from the magnetite-group IOA deposits have relatively high Mg, Co, and V contents and low Si, Ca, W, Sn, Nb, and Mo contents, whereas those from the magnetite + hematite-group IOA deposits have relatively high W, Sc, and Ti contents but low Al, Mg, and Zn contents (Fig. 6b).

EPMA analyses show that iron oxides from the high-temperature Ca–Fe alteration have relatively high Mg, V, and Ni contents, but relatively low K and Al contents (Fig. 6c). Iron oxides from high-temperature K–Fe alteration have relatively high Mn and Cr contents, whereas those from low-temperature K–Fe alteration have relatively high Si, Ca, Sn, Cu, and Ti contents but relatively low Mn, Mg, V, and Ni

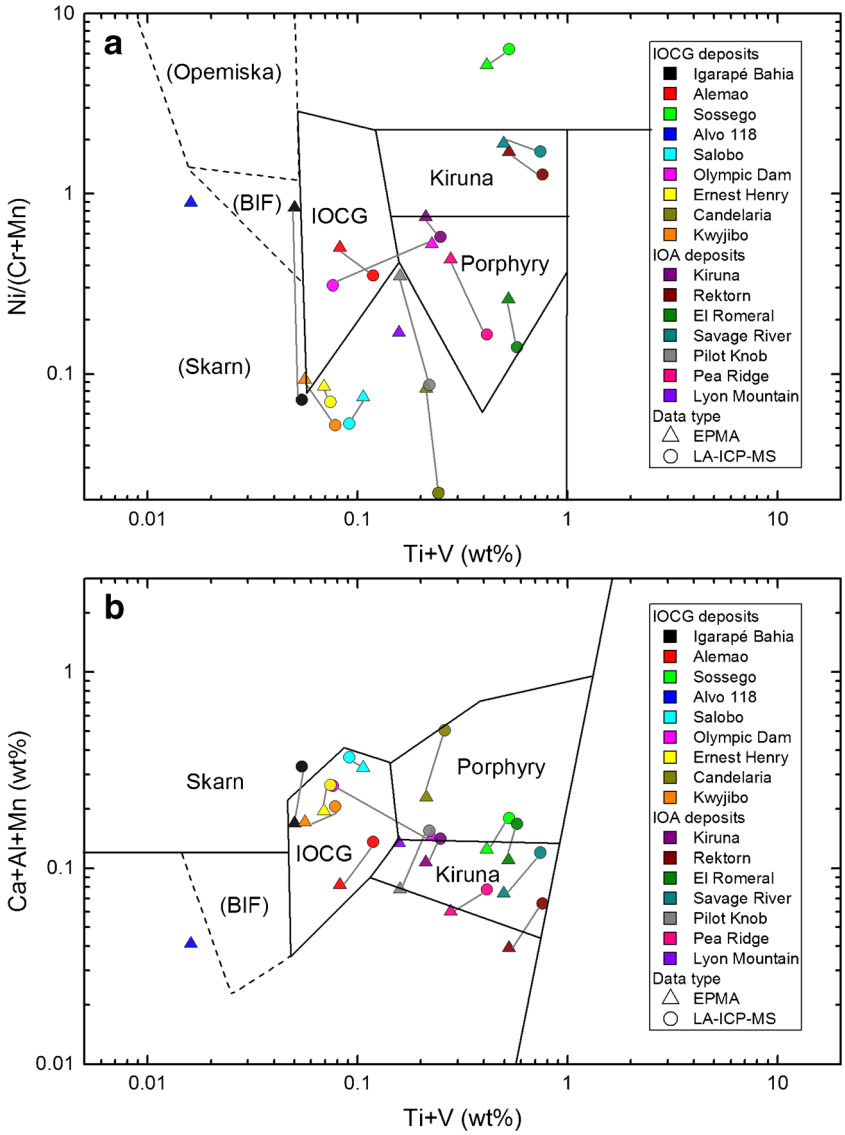

Fig. 5 Plot of EPMA and LA-ICP-MS data of IOCG and IOA deposits in the Ti + V vs. Ni/(Cr + Mn) (**a**) and Ti + V vs. Ca + Al + Mn (**b**) (Dupuis and Beaudoin 2011). *BIF* banded iron formation, *Skarn* Fe–Cu skarn deposits, *IOCG* iron oxide–copper–gold deposits, *Porphyry* porphyry Cu deposits, *Kiruna* Kiruna apatite–magnetite deposits. Gray line links EPMA and LA-ICP-MS average compositions for the same deposit

contents (Fig. 6c). LA-ICP-MS analyses show that iron oxides from high-temperature Ca–Fe alteration have relatively high Mg, Ti, Co, V, and Ni contents and low Ca, Al, Ge, Sn, Cu, and Mo contents (Fig. 6d). Iron oxides from high-temperature K–Fe alteration have relatively high Mn, Zn, and Cr contents but low Zr, W, and Nb contents, whereas those from the low-temperature K–Fe alteration have relatively high Si, Ca, Pb, Zr, W, Sn, Nb, Cu, and Mo contents but low Ga, Mn, Mg, Ti, Co, V, Ni, and Cr contents (Fig. 6d).

PLS-DA results of iron oxide composition

Host rocks

The studied deposits are divided into three groups according to the types of host rocks, volcano-sedimentary rocks, volcanic rocks, and granitic rocks (Online Resource 1). Figure 7 shows the PLS-DA results of EPMA and LA-ICP-MS data of iron oxides classified by different host rocks. PLS-DA of iron oxide EPMA data shows that despite forming overlapping clusters in t_1–t_2, samples hosted by granitic rocks plot in the right side of t_1 due to correlated Si, Ti, and Al and inversely correlated to V (Fig. 7a, b). Iron oxides hosted by volcanic rocks are discriminated by correlated V and Mn from those hosted by volcano-sedimentary rocks that show Mg and Si covariation (Fig. 7a, b). The overlapping of iron oxide compositions divided by types of rocks in t_1–t_2 (Fig. 7b) indicates that EPMA Si, Ca, Mg, Mn, Al, Ti, and V values are poor discriminators for host rocks. PLS-DA of LA-ICP-MS data shows that samples with more elemental variables result in better separation of iron oxides from different host rocks. Samples hosted by granitic rocks are characterized by correlated Pb, Ge, Sn, Cu, Mn, and Zn (Fig. 7c) and negative

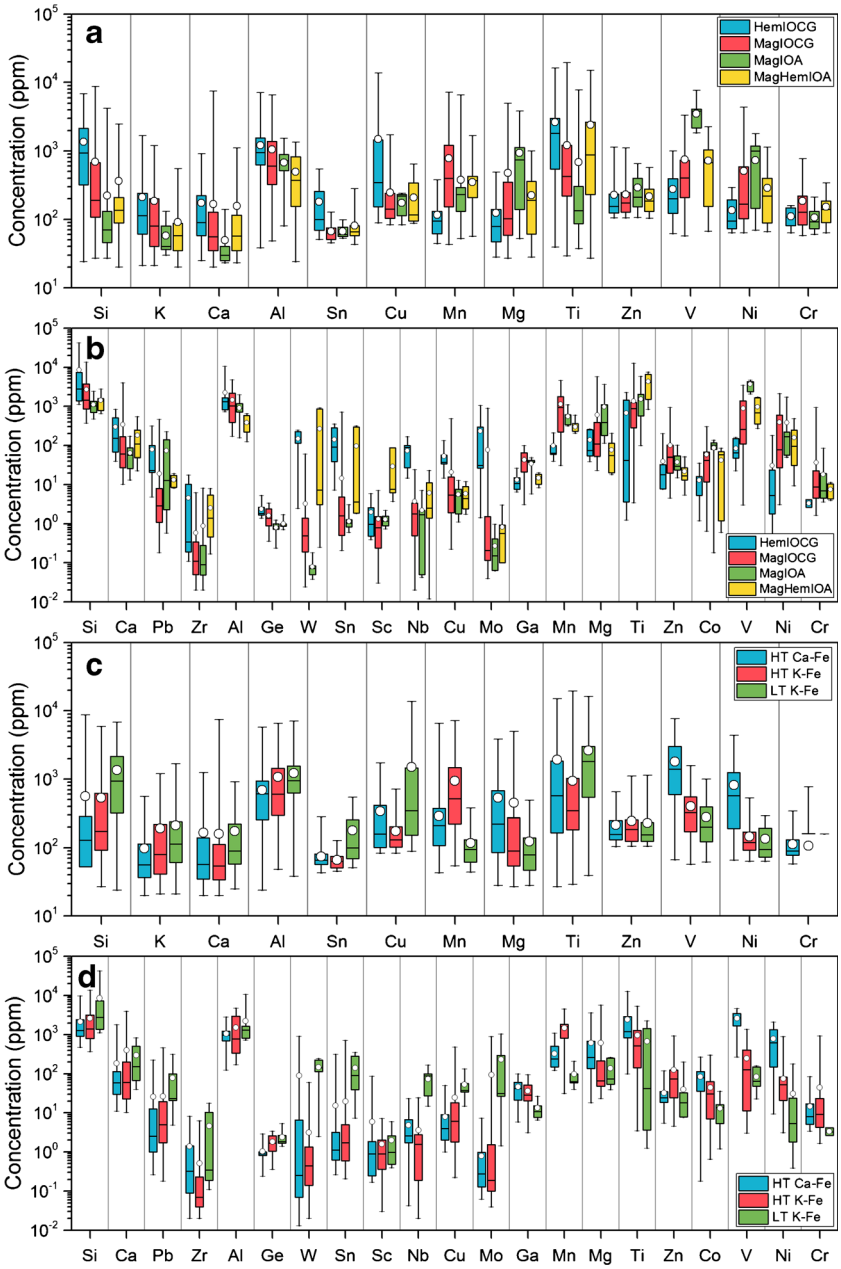

Fig. 6 Multi-element box and whisker plots for EPMA and LA-ICP-MS trace element data of iron oxides from different deposit subtypes (**a**, **b**) and alteration types (**c**, **d**). Boxes outline the 25th to 75th percentiles and whiskers extend to the minimum and maximum values. Short line within the box represents the median value, whereas circle filled by white on the whisker represents the average value. Trace element contents below the limit of detection were removed from the box and whisker plots. *HemIOCG* hematite-group IOCG deposits, *MagIOCG* magnetite-group IOCG deposits, *MagIOA* magnetite-group IOA deposits, *MagHemIOA* magnetite + hematite-group IOA deposits, *HT Ca-Fe* high-temperature Ca–Fe alteration, *HT K-Fe* high-temperature K–Fe alteration, *LT K–Fe* low-temperature K–Fe alteration

t_2 values (Fig. 7d). Samples hosted by volcano-sedimentary rocks plot in the negative side of t_1 due to correlated Nb, Mo, Ni, and Cr, whereas samples hosted by volcanic rocks plot on the positive side of t_2 due to correlated Pb, Sc, Mg, Ti, and V (Fig. 7c, d).

Deposit types

PLS-DA of EPMA data shows that iron oxides from IOA deposits are positively correlated to Mg and V, whereas those from IOCG deposits are positively correlated to Si and Al (Fig. 8a, b). IOCG and IOA deposits can be separated in the t_1–t_2 space by Si, Ca, Al, Mn, Mg, Ti, Co, and Ni compositions of iron oxides (Fig. 8b). However, nearly half of IOCG and IOA iron oxide compositions overlap (Fig. 8b) indicating that PLS-DA of EPMA data has limited efficiency in discriminating these two deposit types. In contrast, PLS-DA of LA-ICP-MS data shows that iron oxides from the IOA deposits can be separated from IOCG deposits with slight overlapping due to covariation of Pb, Sc, and V (Fig. 8c, d). Score contribution diagrams for both EPMA (Fig. 8e, f) and LA-ICP-MS (Fig. 8g, h) data show that distinct, opposite chemical signatures separate iron oxides from IOCG deposits from those from IOA deposits. The score contribution plots show that positive contribution of Al, Ge, Si, Nb, Cu, Mo, Ga, and Zn

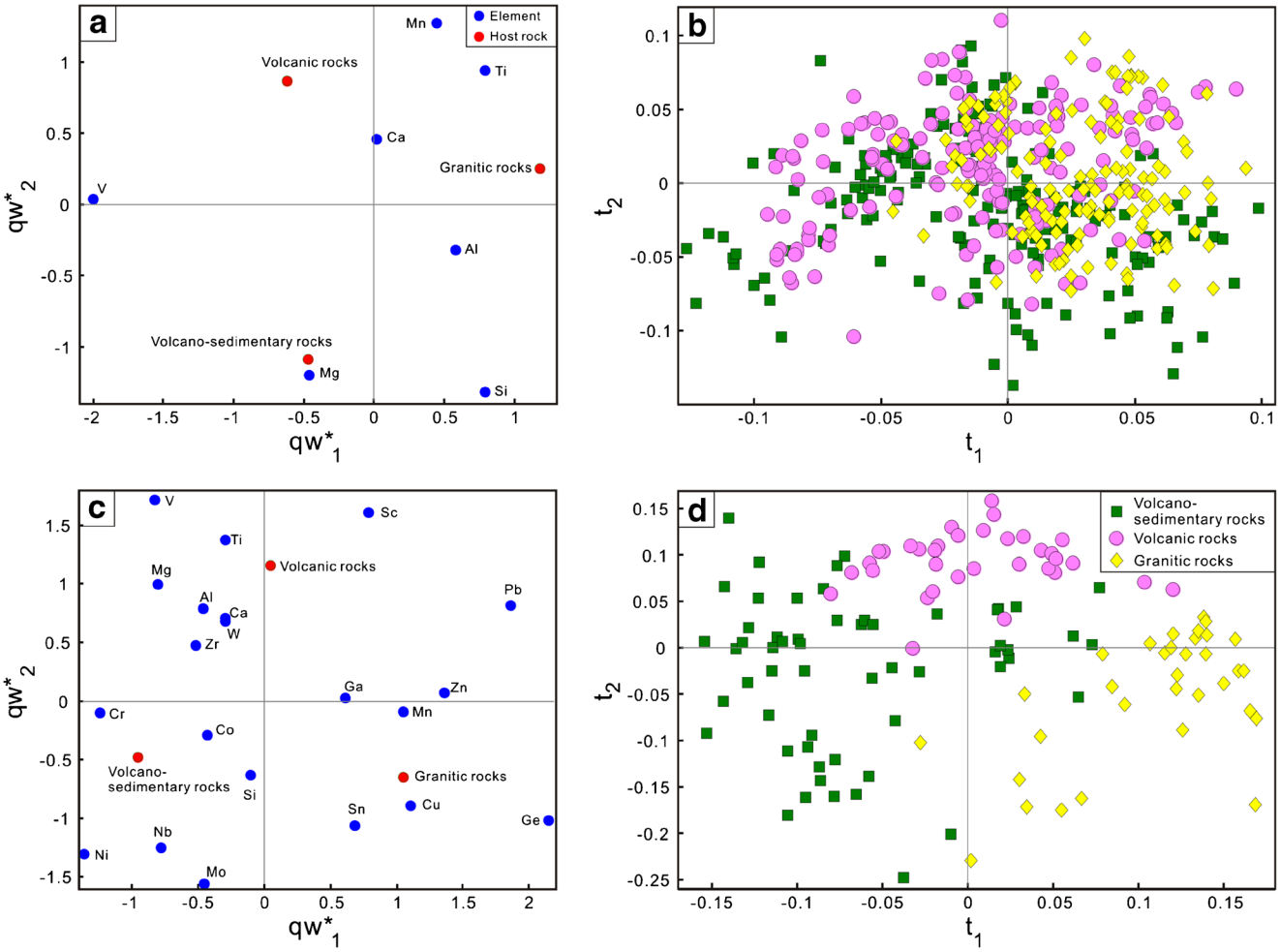

Fig. 7 PLS-DA of EPMA (**a**, **b**) and LA-ICP-MS (**c**, **d**) data of iron oxides grouped by host rocks. **a** The qw^*_1–qw^*_2 (first and second loadings) plot based on EPMA data showing correlations among element variables and host rocks. **b** The t_1–t_2 (first and second scores) plot showing the distribution of individual analyses of samples in the latent variable space defined by qw^*_1–qw^*_2 in (**a**). **c** The qw^*_1–qw^*_2 (first and second loadings) plot based on LA-ICP-MS data showing correlations among element variables and host rocks. **d** The t_1–t_2 (first and second scores) plot showing the distribution of individual analyses of samples in the latent variable space defined by qw^*_1–qw^*_2 in (**c**)

discriminates iron oxides from the IOCG deposits, whereas positive contribution of Pb, Sc, V, and Mg discriminates those from the IOA deposits (Fig. 8e–g).

PLS-DA of EPMA data shows that iron oxides from hematite-group IOCG deposits plot in the left side of t_1–t_2 because of correlated Ca, Ti, and Si, whereas those from magnetite-group IOA deposits plot in the right side of t_1–t_2 due to covariation of Mg and V (Fig. 9a, b). Iron oxides from magnetite + hematite-group IOA deposits are near the center of the scores plot and thus are not well classified (Fig. 9b). Although samples from the magnetite-group IOCG deposits are dispersed in t_1–t_2, their distribution indicates that they are positively correlated to Al and Mn and negatively correlated to V and Mg (Fig. 9a, b). Therefore, PLS-DA of EPMA data efficiently discriminate magnetite-group IOA deposits from other types of deposits, but cannot discriminate magnetite + hematite-group IOA, magnetite-group and hematite-group IOCG deposits. The classification of iron oxide groups from different IOCG and IOA deposits is improved by PLS-DA of LA-ICP-MS data since more elements are used (Fig. 9c, d). Iron oxides from hematite-group IOCG deposits plot in the negative t_1 and t_2 region due to covariation of Nb, Cu, Mo, W,

Fig. 8 PLS-DA results of EPMA and LA-ICP-MS data of iron oxides ▶ from IOCG and IOA deposits. **a** Plot of qw^*_1 vs. qw^*_2 (first and second loadings) based on EPMA data showing correlations among element variables and deposit types. **b** Plot of t_1 vs. t_2 (first and second scores) showing the distribution of individual analyses from different deposit types in the latent variable space defined by qw^*_1–qw^*_2 in (**a**). **c** Plot of qw^*_1 vs. qw^*_2 (first and second loadings) based on LA-ICP-MS data showing correlations among element variables and deposit types. **d** Plot of t_1 vs. t_2 (first and second scores) showing the distribution of individual analyses from different deposit types in the latent variable space defined by qw^*_1–qw^*_2 in (**c**). **e**–**h** Score contribution plots of elements for IOCG and IOA deposits

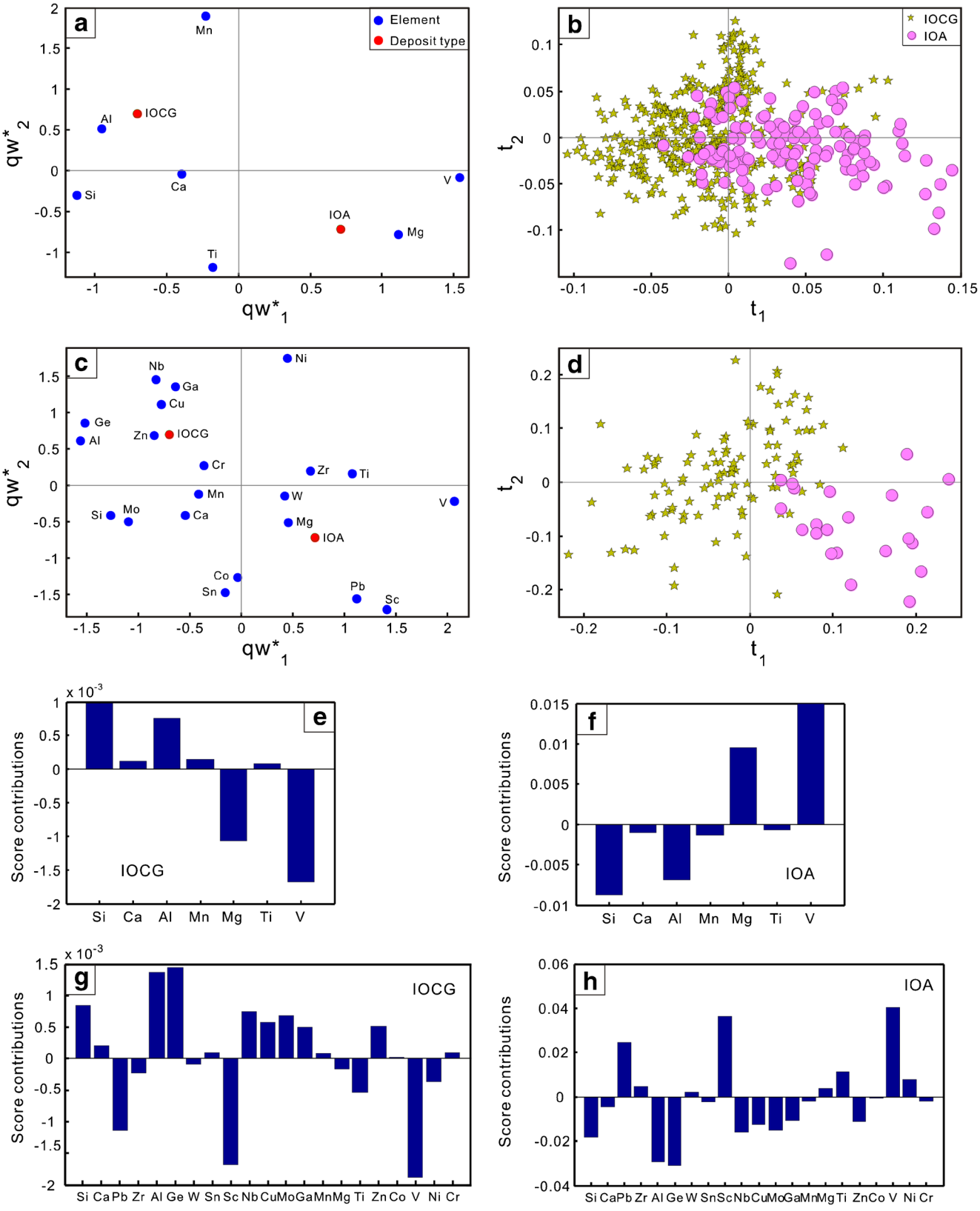

and Sn, whereas those from magnetite + hematite-group IOA deposits plot in the negative t_1, positive t_2 region, due to covariation of Sc, Pb, and Zr (Fig. 9c, d). Iron oxides from hematite-group IOCG deposits can be separated from those of

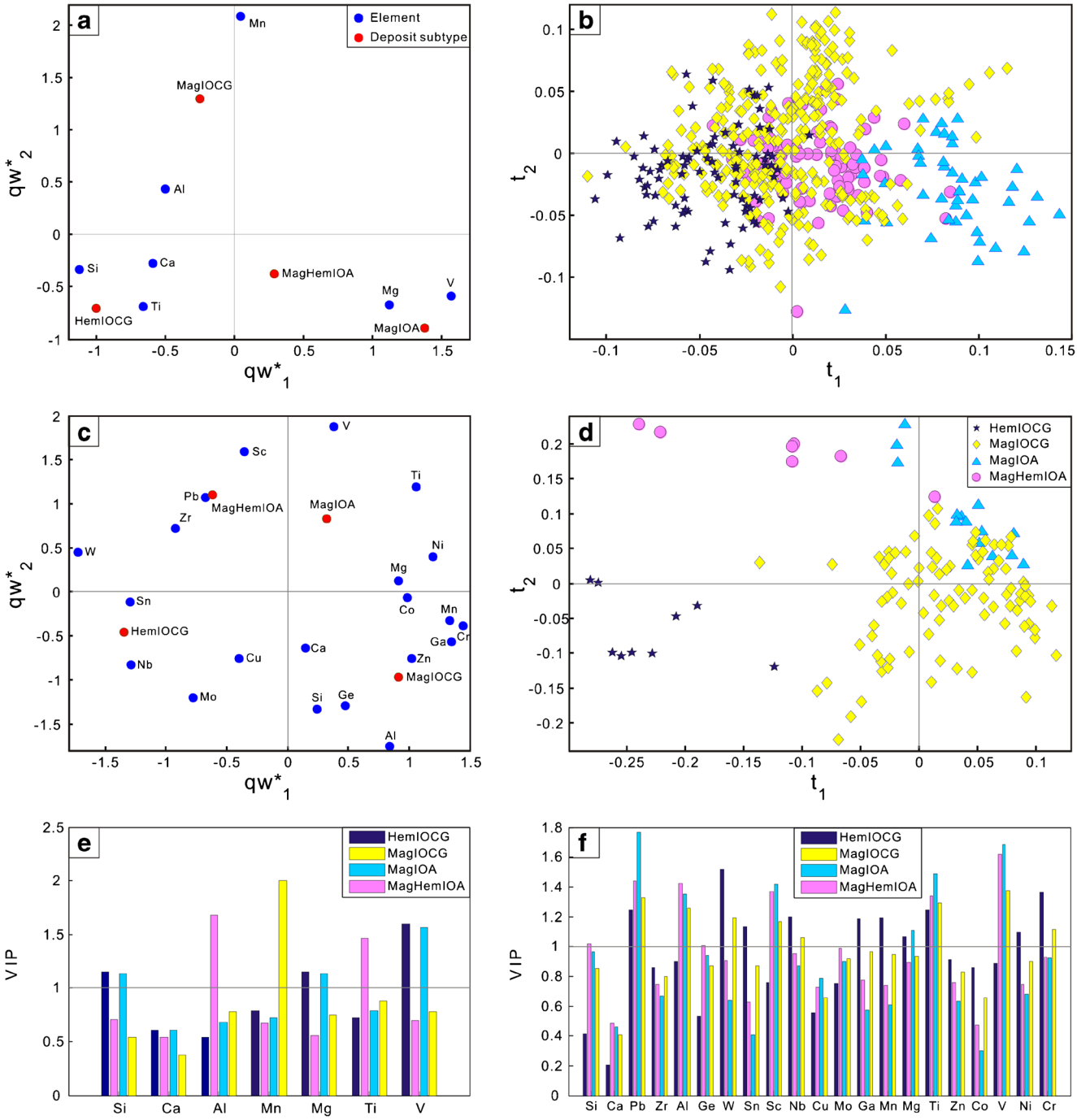

Fig. 9 PLS-DA results of EPMA and LA-ICP-MS data of iron oxides from different subtypes of IOCG and IOA deposits. **a** Plot of qw^*_1 vs. qw^*_2 (first and second loadings) based on EPMA data showing correlations among element variables and deposit subtypes. **b** Plot of t_1 vs. t_2 (first and second scores) showing the distribution of individual analyses of samples from different deposit subtypes in the latent variable space defined by qw^*_1–qw^*_2 in (**a**). **c** Plot of qw^*_1 vs. qw^*_2 (first and second loadings) based on LA-ICP-MS data showing correlations among element variables and deposit subtypes. **d** Plot of t_1 vs. t_2 (first and second scores) showing the distribution of individual analyses of samples from different deposit subtypes in the latent variable space defined by qw^*_1–qw^*_2 in (**c**). **e** The VIP showing the importance of compositional variables in classification of samples in (**b**). **f** The VIP showing the importance of compositional variables in classification of samples in (**d**). Gray lines in (**e**) and (**f**) represent the VIP value of 1. Elements with VIP value higher than 1 are the most important in the classification. *HemIOCG* hematite-group IOCG deposits, *MagIOCG* magnetite-group IOCG deposits, *MagIOA* magnetite-group IOA deposits, *MagHemIOA* magnetite + hematite-group IOA deposits

magnetite + hematite-group IOA deposits and magnetite-group IOA deposits by t_2 (Fig. 9d). Iron oxides from magnetite-group IOA deposits plot in the high, positive t_1 side due to covariations of Pb and V (Fig. 9d). Iron oxides

from magnetite-group IOCG deposits show a diverse composition and overlap the field of magnetite-group IOA deposits (Fig. 9d). VIP plot for PLS-DA of EPMA data in Fig. 9b indicates that Si, Mg, and V are important elements discriminating hematite-group IOCG deposits and magnetite-group IOA deposits (Fig. 9e). Aluminum and Ti are the most important elements to distinguish between magnetite + hematite-group IOA deposits, whereas Mn is the important element for discriminating magnetite-group IOCG deposits (Fig. 9e). The VIP diagram for PLS-DA of LA-ICP-MS data in Fig. 9d indicates that Pb and Ti are important factors discriminating all the deposit subtypes (Fig. 9f). In separation of hematite-group IOCG deposits, Sn, Ga, Mn, and Ni are the most important, whereas Al and Sc are important for other three deposit subtypes (Fig. 9f). Tungsten, Nb, and Cr are important variables discriminating hematite-group IOCG deposits and magnetite-group IOCG deposits (Fig. 9f).

Alteration types

PLS-DA of EPMA data (Fig. 10a, b) shows that iron oxides formed by high-temperature and low-temperature K–Fe alteration are separated by qw^*_1 from those formed by high-temperature Ca–Fe alteration (Fig. 10a). Despite the formation of overlapping clusters in Fig. 10b, iron oxides from high-temperature Ca–Fe alteration mostly plot in the high t_1 region because of correlated Mg and V, whereas those from low-temperature K–Fe alteration have negative t_1 values due to covariation of Si, Ca, and Ti (Fig. 10a, b). Variation in Mn, Si, and Ti compositions of iron oxides separate high- and low-temperature K–Fe alteration classes (Fig. 10a). In comparison with the EPMA data, PLS-DA of LA-ICP-MS data results in a better classification of samples of various alteration types (Fig. 10b). This is likely due to the larger number of LA-ICP-MS variables. Samples from the high-temperature Ca–Fe alteration are characterized by covariation of V and Ni (Fig. 10c) and plot in the positive t_1 and t_2 region (Fig. 10d), whereas low-temperature K–Fe alteration shows correlated Nb, W, and Zr (Fig. 10c) and plot in the positive t_1 and negative t_2 region (Fig. 10d). Samples from high-temperature K–Fe alteration plot in the negative t_2 side due to correlated Mn, Ge, Cr, and Zn (Fig. 10c, d). The VIP plot for PLS-DA of EPMA data in Fig. 10a indicates that Mn and V are the most important elements in the classification of all classes (Fig. 10e). The VIP plot for PLS-DA of LA-ICP-MS data shows that V and Ni are main contributors in separation of different sample classes in Fig. 10d. Germanium, W, Mn, and Zn are discriminants for both high-temperature Ca–Fe and K–Fe alteration (Fig. 10f), whereas Pb, Sn, Nb, Mo, and Ti are the most important elements in the classification of low-temperature K–Fe alteration (Fig. 10f).

Discussion

Magnetite and hematite from IOCG and IOA deposits contain minor and trace elements from below detection limit to a few percent. These elements are structurally incorporated into magnetite/hematite or form micrometer to nanometer mineral inclusions (Lindsley 1976; Wechsler et al. 1984; Huberty et al. 2012; Xu et al. 2014; Nadoll et al. 2014; Deditius et al. 2018). Magnetite has an inverse spinel structure with the general formula AB_2O_4, where A is divalent and B is trivalent. Nadoll et al. (2014) summarized common cations that can substitute for Fe^{3+} in the tetrahedral sites and Fe^{2+}/Fe^{3+} in the octahedral sites according to Goldschmidt's rule (Goldschmidt 1958). They suggested that Mg, Mn, Zn, Co, and Ni may substitute for Fe^{2+}, whereas Al, Ga, and As substitute for Fe^{3+} (Nadoll et al. 2014). Tetravalent ions such as Ti^{4+} may occupy the Fe^{3+} site by coupled substitution with a divalent cation (Wechsler et al. 1984). Vanadium, Cr, and Mn have different valences, and their incorporation depends on oxygen fugacity (Lindsley1976; Sievwright et al. 2017; Sossi et al. 2018). Relatively high trace element contents in zoned magnetite from the Los Colorados IOA deposit have been shown to contain micrometer to nanometer mineral inclusions (Deditius et al. 2018). Nanometer-scale particles in trace element-rich zones are caused by local mineral supersaturation in hydrothermal fluids during crystallization of host magnetite (Deditius et al. 2018). If the inclusions formed under equilibrium conditions, then the micrometer-scale domains sampled by EPMA and LA-ICP-MS should provide information about the fluid composition. In contrast, if inclusions formed under disequilibrium conditions, then large variations in trace element contents are expected to characterize the iron oxide composition measured by EPMA and LA-ICP-MS.

Iron oxide trace element composition of IOCG (Carew 2004; Rusk et al. 2009, 2010; Dupuis and Beaudoin 2011; Zhang et al. 2011; Acosta-Góngora et al. 2014; Chen et al. 2015; De Toni 2016) and IOA (Müller et al. 2003; Knipping et al. 2015a, b; Heidarian et al. 2016; Velasco et al. 2016; Broughm et al. 2017) deposits have been reported. In most studies, the trace element composition of iron oxides is used to discuss the factors controlling compositional variations and the formation of mineralization. In addition, based on compositional differences between ore-related and barren magnetite, it can be used as an indicator mineral in the exploration for IOCG deposits (Carew 2004; Rusk et al. 2009, 2010; Acosta-Góngora et al. 2014). Dupuis and Beaudoin (2011) investigated trace element compositions of magnetite and hematite from ten IOCG and seven IOA deposits using EPMA and constructed binary diagrams to discriminate these deposit types. However, due to the detection limits of EPMA, several trace elements in magnetite and hematite could not be

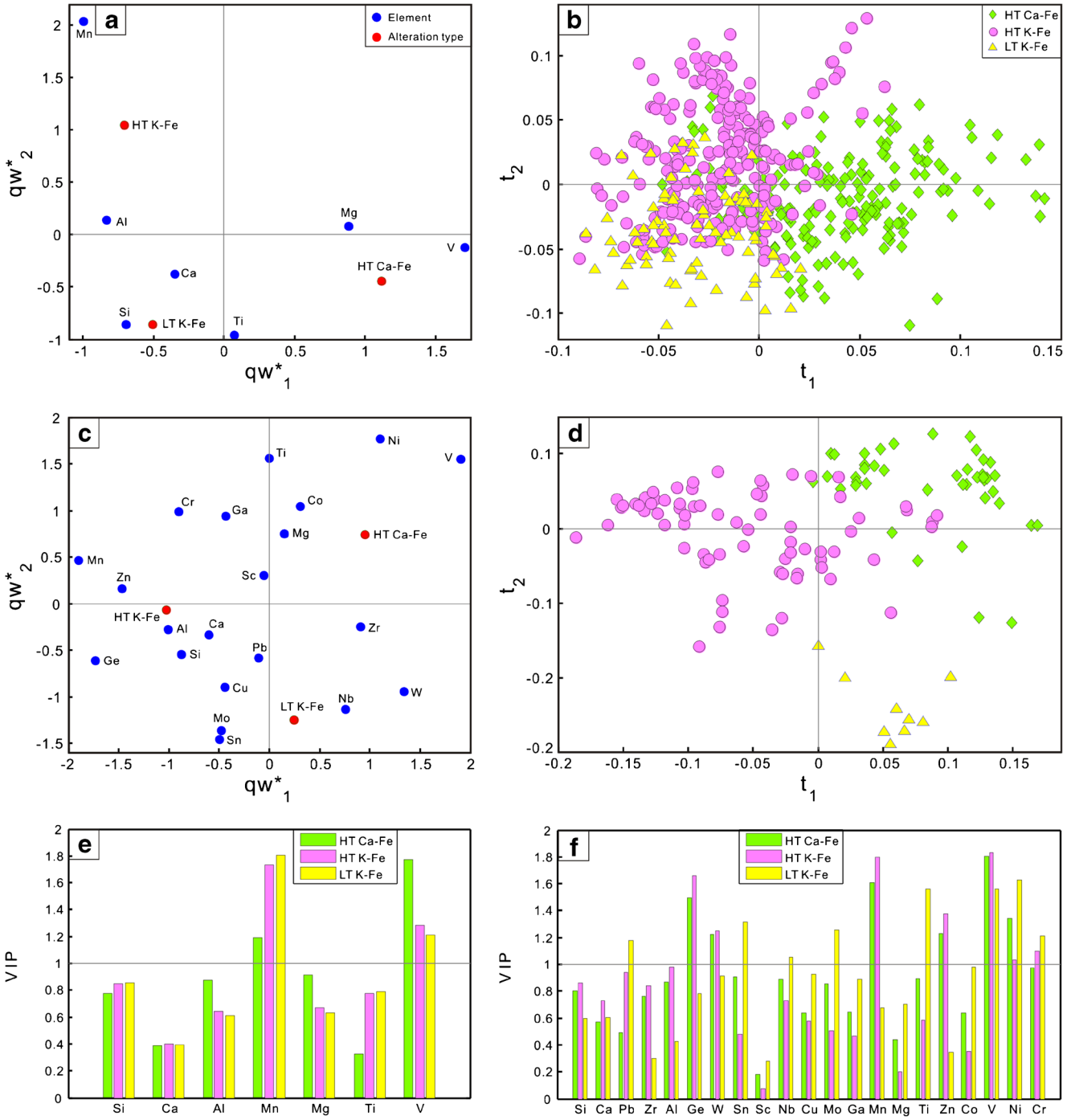

Fig. 10 PLS-DA results of EPMA and LA-ICP-MS data of iron oxides from different alteration types. **a** Plot of qw^*_1 vs. qw^*_2 (first and second loadings) based on EPMA data showing correlations among element variables and alteration types. **b** Plot of t_1 vs. t_2 (first and second scores) showing the distribution of individual analyses of samples from different alteration types in the latent variable space defined by qw^*_1–qw^*_2 in (**a**). **c** Plot of qw^*_1 vs. qw^*_2 (first and second loadings) based on LA-ICP-MS data showing correlations among element variables and alteration types. **d** Plot of t_1 vs. t_2 (first and second scores) showing the distribution of individual analyses of samples from different alteration types in the latent variable space defined by qw^*_1–qw^*_2 in (**c**). **e** The VIP showing the importance of compositional variables in classification of samples in (**b**). **f** The VIP showing the importance of compositional variables in classification of samples in **d**. Gray lines in (**e**) and (**f**) represent the VIP value of 1. Elements with VIP value higher than 1 are the most important in the classification. *HT Ca–Fe* high-temperature Ca–Fe alteration, *HT K–Fe* high-temperature K–Fe alteration, *LT K–Fe* low-temperature K–Fe alteration

measured. Moreover, some magnetite in IOA deposits experienced re-equilibration processes, complicating the application of these discrimination diagrams (Heidarian et al. 2016; Broughm et al. 2017). Acosta-Góngora et al.

(2014) and De Toni (2016) linked trace element data of magnetite from IOCG deposits in the Great Bear magmatic zone (Canada) to IOCG alteration types. However, due to limited data and alteration types, the relationship between magnetite chemistry and alteration types needs further constraints. Thus, this study combines EPMA and LA-ICP-MS data of magnetite and hematite from worldwide IOCG and IOA deposits to discuss the controlling factors of the iron oxide chemistry and its relationship to alteration types and IOCG and IOA deposit subtypes.

Comparison of magnetite and hematite composition

For most IOCG and IOA deposits, magnetite is commonly replaced by hematite to form martite, whereas the replacement of hematite by magnetite (mushketovite) is less common. It has been shown that most spinel-forming elements, except Mg, are retained during martitization under moderate-temperature hydrothermal oxidation (Sidhu et al. 1981; Angerer et al. 2012). However, Cornell and Schwertmann (2003) showed that the martitization process can expel divalent cations due to their incompatible valency and ionic radii. The reduction of hematite to magnetite involves reductive dissolution of hematite iron to $Fe^{2+}_{(aq)}$ followed by non-redox reaction of hematite and $Fe^{2+}_{(aq)}$ to magnetite in low temperature (100–250 °C) hydrothermal systems (Ohmoto 2003; Otake et al. 2010). In high-temperature hydrothermal environment (350–570 °C), hematite can be transformed to magnetite via reductive dissolution of hematite by hydrogen or iron metal (Matthews 1976). Magnetite and hematite from IOA deposits, Rektorn, Pea Ridge, Pilot Knob, and Lyon Mountain, show similar bulk continental crust normalized trace element patterns (Online Resource 6). This indicates that magnetite and hematite in a deposit share the same origin. Oxygen fugacity-sensitive elements, such as V, also show indistinguishable concentrations between magnetite and hematite from these deposits (Online Resource 6), implying relatively stable oxygen fugacity conditions or transformation of magnetite–hematite by non-redox reactions (Swann and Tighe 1977; Ohmoto 2003). This conclusion is similar to previous results showing no systematic variations in trace element composition between magnetite and hematite at a deposit scale (Dupuis and Beaudoin 2011; Huang et al. 2015b). Considering the similar chemical composition of magnetite and hematite in a deposit, they are discussed together thereafter.

Effect of oxygen fugacity and temperature on iron oxide chemistry

As reviewed by Nadoll et al. (2014), various factors likely control trace element incorporation in hydrothermal magnetite from different types of deposits. Although there are limited studies on the partitioning of trace elements between magnetite and hydrothermal fluids (Ilton and Eugster 1989), it is generally considered that the same factors controlling trace elements in igneous-derived magnetite (e.g., fluid/melt composition, temperature, pressure, cooling rate, oxygen fugacity, sulfur fugacity, and silica activity) also control partitioning of trace elements in magnetite under high- to low-temperature hydrothermal conditions, with the additional parameter of fluid–rock reactions (Putnis and Austrheim 2013; Dare et al. 2014; Nadoll et al. 2014). Vanadium and Sn can occur in various valency states (V^{3+}, V^{4+}, V^{5+}, Sn^{2+}, Sn^{4+}) and, as such, are sensitive to oxygen fugacity in silicate melts (Goldschmidt 1958; Toplis and Corgne 2002; Righter et al. 2006; Sievwright et al. 2017). For example, increasing oxygen fugacity decreases the partition coefficient of V, but not of Co and Ni, for magnetite in an iron-rich melt/liquid (Toplis and Corgne 2002; Righter et al. 2006; Sievwright et al. 2017), whereas Sn is readily partitioned into magnetite under more oxidized condition (Goldschmidt 1958; Carew 2004). Carew (2004) ascribed the decreasing V concentration in magnetite from K–Fe alteration to Cu–Au mineralization at Ernest Henry to a progressive increase in oxygen fugacity of fluids. From high-temperature Ca–Fe to K–Fe, and to low-temperature K–Fe alteration, V contents in iron oxides decrease and Sn contents increase (Fig. 6c, d), which may be due to the decreasing temperature and increasing oxygen fugacity during the evolution of hydrothermal alteration (Corriveau et al. 2016). Moreover, iron oxides from magnetite-group IOCG deposits, regarded to form at higher temperature (generally > 350 °C) and under relatively more reducing conditions (Williams 2010a), have higher V and lower Sn contents than those from hematite-group IOCG deposits (Fig. 6a, b), which are considered to have formed at lower temperature (~ 200–350 °C) and under relatively more oxidized conditions (Williams 2010a). Similarly, iron oxides from magnetite-group IOA deposits have higher V and lower Sn contents than those from magnetite + hematite-group IOA deposits (Fig. 6a, b). These regular variations in V and Sn contents between different deposit subtypes are most likely due to the evolving oxygen fugacity and temperature of the hydrothermal systems.

Effect of co-precipitating minerals on iron oxide chemistry

Minerals co-crystallizing with iron oxides will affect their trace element composition. For example, sulfide minerals preferentially incorporate chalcophile (e.g., Cu, Pb, Zn, As, Ag, Sb) and siderophile elements (e.g., Ni, platinum-group elements) (Cygan and Candela 1995; Fleet et al.

1996; Simon et al. 2008), whereas lithophile elements, such as Mg, Al, and Ti, partition into silicates (Frost 1991; Toplis and Corgne 2002). For magnetite crystallized from a Fe-rich sulfide liquid, Ni, Co, Zn, Mo, Sn, and Pb have lower abundance in co-precipitating magnetite because these elements partition into co-crystallizing sulfides (Dare et al. 2012). Because Ni, Mo, and Co are compatible in Fe-rich monosulfide solution (MSS) but incompatible in Cu-rich intermediate solid solution (ISS), magnetite crystallized from MSS is depleted in these elements relative to those crystallized from Cu-rich ISS in which Fe-sulfides are scarce (Dare et al. 2012). Such behavior is also observed within metasomatic systems. For example, at the Kwyjibo deposit, magnetite (sample KJ2) associated with chalcopyrite and pyrite has lower Co content, but similar Ni, than magnetite (samples KJ1, 3) associated with chalcopyrite only (Online Resources 5 and 6), suggesting that co-precipitating pyrite can significantly affect the Co content in magnetite. This is consistent with previous conclusions of Carew (2004) and Huang et al. (2014) that the presence or absence of pyrite in the mineral assemblage significantly affects the Co content, but has little effect on Ni in magnetite. It is also consistent with pyrite (and arsenopyrite) in mineral assemblages with Co-rich and Cu-deficient metal associations in high-temperature Ca–K–Fe alteration (Corriveau et al. 2016, 2017). Compared to IOCG deposits, sulfide-deficient IOA deposits iron oxides are co-precipitated with minor Fe-dominant sulfides, yielding iron oxides with higher Pb and Ni contents (Fig. 8c, d), suggesting that Pb and Ni in IOCG iron oxides are depleted by co-precipitating pyrite and/or pyrrhotite. However, the higher Cu, Mo, and Zn contents in IOCG iron oxides are inconsistent with partitioning in co-precipitating sulfides. This may be due to the fact that the Cu-bearing sulfides tend to be paragenetically later than magnetite in IOCG system (Williams et al. 2005; Zhao and Zhou 2011).

Effect of host rocks on iron oxide chemistry

The relative enrichment of Mg ± Mn in sample F392 from the Igarapé Bahia deposit, sample 11CC051 from the Salobo deposit, and sample Ehenry2 from the Ernest Henry deposit (Online Resource 5) could reflect differences in fluid chemistry and the evolution of the alteration facies. It has been demonstrated that elements such as Mg and Mn can be progressively enriched in hydrothermal fluids by extensive fluid/rock interactions (Einaudi et al. 1981; Meinert et al. 2005), which is reflected in high Mg, Mn, Ca, and Si concentrations in skarn magnetite (Acosta-Gongora et al. 2014; Dupuis and Beaudoin 2011; Nadoll et al. 2015; Zhao and Zhou 2015; Huang et al. 2016). In parallel, it has been demonstrated that in evolving iron oxide alkali–calcic alteration systems, early skarn with high Mg is gradually replaced by the high-temperature Ca–Fe alteration facie, resulting in leaching of Mg from skarn and its transfer to the fluid (Corriveau et al. 2016, 2017). The varying degrees of interaction between hydrothermal fluids and carbonate country rocks of skarn deposit and their subsequent replacement by more evolved alteration facies can thus explain the various Mg and/or Mn contents of samples in one deposit.

Concentrations of V, Co, Ni, and Cr in magnetite can reflect the composition of host rocks and of the alteration facies (Carew 2004; Acosta-Góngora et al. 2014; Dare et al. 2014; Corriveau et al. 2016, 2017). Lack of geochemical data for host rocks of the studied samples prevents comparison with iron oxide compositions. The host rocks have an original control on alteration facies as well as on the metal budget of fluids through extensive leaching of host rocks during early albitization and high-temperature Ca–Fe alteration facies (Corriveau et al. 2016, 2017), which impact on iron oxide chemistry as shown by the PLS-DA results (Fig. 7). Samples hosted in granitic rocks are characterized by higher Pb, Ge, Sn, Cu, Mn, and Zn contents and lower V, Ni, and Cr contents (Fig. 7c, d), which is consistent with magnetite precipitated from metasomatic alteration related to granitic host rocks, which has elevated W, Pb, As, Mo, and Sn (Nadoll et al. 2014). Samples hosted by volcano-sedimentary and volcanic rocks can be discriminated by higher V, Ni, and Cr (Fig. 7d), indicating that iron oxide chemistry is partly dependent on the host rock composition of systems hosting IOCG and IOA deposits.

Relationship between deposit subtypes and iron oxide chemistry

In this section, we link the chemical composition of iron oxides with deposit subtypes defined by Williams (2010a). Iron oxides from different subtypes of IOCG and IOA deposits have different trace element compositions. Iron oxides from the hematite-group IOCG deposits are characterized by high Si, K, Ca, Al, Pb, Zr, Ge, W, Sn, Sc, Nb, Cu, and Mo but low Ga, Mn, Mg, Zn, Co, V, and Ni, whereas those from magnetite-group IOCG deposits have relatively low Pb, Zr, and Hf and high Ga, Mn, Zn, Ni, and Cr (Fig. 6a, b). Hematite-group IOCG deposits are typically associated with sericite and/or chlorite–(quartz–albite–carbonate) alteration that developed at temperatures between 200 and 350 °C, whereas magnetite-group IOCG deposits formed in deeper crustal settings and are associated with medium to high temperature (generally > 350 °C) silicate alteration assemblages (Williams et al. 2005; Corriveau et al. 2010, 2016). The relative depletion of compatible elements (Ga, Mn, Zn, Co, Ni, Cr) in hematite-group IOCG deposits iron oxides most likely results from the lower

temperature solubility of these elements in fluids (Nadoll et al. 2012, 2014; Dare et al. 2014). As discussed above, the higher Sn, and lower V, in iron oxides from the hematite-group IOCG deposits are due to higher oxygen fugacity. Higher contents of incompatible elements (Zr, Ge, W, Sn, Sc, Nb, Cu) in iron oxides from the hematite-group IOCG deposits may partly result from reaction with granitic host rocks or water/rock exchange. Iron oxides from the magnetite-group IOA deposits have relatively high Mg, Co, and V and low Si, K, Ca, W, Sn, Nb, and Mo contents, whereas those from magnetite + hematite-group IOA deposits have relatively high Zr, W, Sn, Sc, and Ti, but low Al and Mg contents (Fig. 6a, b). The compositional differences between iron oxides from magnetite-group and magnetite + hematite-group IOA deposits may be also due to different temperature and oxygen fugacity.

PLS-DA of EPMA and LA-ICP-MS iron oxide compositional data shows that hematite-group IOCG deposits, magnetite-group and magnetite + hematite-group IOA deposits have distinct compositional characteristics (Fig. 9b, d). Iron oxides from magnetite-group IOCG deposits show a compositional diversity and overlap with those from hematite-group and magnetite + hematite-group IOCG deposits (Fig. 9b). Magnetite-group IOCG deposits have diverse silicate alteration assemblages, including high temperature K–Fe–(Mn–Ba) and high temperature Ca–Fe–Mg–(Na) (Williams 2010a). For samples in this study, magnetite-group IOCG deposits cover both high-temperature K–Fe and Ca–Fe alteration types (Online Resource 2). These two alteration types have different geochemical signatures (Montreuil et al. 2013; Corriveau et al. 2016, 2017), which are also recorded in iron oxide composition (Fig. 10b, d). Therefore, the diverse chemical composition of magnetite-group IOCG deposits may partly result from prograding alteration from the high-temperature Ca–Fe or Ca–K–Fe to high-temperature K–Fe alteration facies.

Relationship between alteration types and iron oxide chemistry

Corriveau et al. (2010, 2016) and Montreuil et al. (2013, 2016) demonstrated that each alteration type of IOCG systems in the Great Bear magmatic zone has a systematic and diagnostic geochemical signature, which is largely independent of the protolith. In general, K and K–Fe alteration is rich in K, Al, Ba, Si, Rb, Zr, Ta, Nb, Th, and U, whereas Ca–Fe alteration is rich in Ca, Fe, Mn, Mg, Zn, Ni, and Co (Montreuil et al. 2013). In addition, transitional alteration facies (high-temperature Ca–K–Fe, skarns, and K-skarns) have been shown to have distinct mineral and metal associations (Corriveau et al. 2016, 2017). In this section, we relate iron oxide chemistry to IOCG alteration types defined by Corriveau et al. (2010, 2016) and evaluate whether the chemical composition of magnetite can serve as a proxy of geochemical signatures of hydrothermal alteration types.

As shown in Fig. 6c, d, iron oxides from the high-temperature Ca–Fe (including some transitional high-temperature Ca–K–Fe), high-temperature K–Fe, and low-temperature K–Fe alteration facies have characteristic trace element compositions. The relative enrichment of Mg, Co, and Ni in iron oxides from the high-temperature Ca–Fe alteration facies is consistent with the interpretation that fluids forming Ca–Fe alteration are rich in Ca, Fe, Mn, Mg, Zn, Ni, and Co (Montreuil et al. 2013; Corriveau et al. 2016). The relative enrichment of Si, K, and Al in iron oxides from both high-temperature and low-temperature K–Fe alteration is consistent with these hydrothermal fluids being rich in K, Al, Ba, Si, Rb, Zr, Ta, Nb, Th, and U (Montreuil et al. 2013).

PLS-DA results of EPMA data show that iron oxides from the high-temperature Ca–Fe alteration can be separated from high-temperature and low-temperature K–Fe alteration due to correlated Mg and V and inversely correlated Si, Al, and Mn (Fig. 10a, b). This is consistent with the average trace element composition of iron oxides for different types of alteration (Fig. 6c, d). Iron oxides from low-temperature K–Fe alteration can be discriminated from high-temperature K–Fe alteration due to correlated W, Sn, Nb, Mo, and Zr (Fig. 10c, d). This indicates that trace element composition of iron oxides reflect fluid composition that evolved to form various alteration types.

Relationship between IOCG and IOA deposits

The relationship between IOCG and IOA deposits remains open to debate. The IOA deposits were classified as a subtype of IOCG deposits in terms of their similarities in tectonic setting, association with igneous activity, mineralogy, and alteration (Hitzman et al. 1992). IOCG and IOA deposits are also considered to represent similar products of magmatic–hydrothermal systems derived from high-temperature calc-alkaline melts variably contaminated by Fe–P–Si-rich crustal rocks and evolving to A-type granites (Hitzman et al. 1992; Rhodes et al. 1999; Sillitoe and Burrows 2002; Corriveau et al. 2007; Tornos 2011). Based on trace element geochemistry of magnetite, Broughm et al. (2017) suggested that magnetite–apatite ores at Kiruna formed from hydrothermal fluids or by post-ore metamorphic or metasomatic alteration. In contrast to the hydrothermal model, a magmatic model was proposed for the formation of IOA deposits where magnetite was crystallized from high-temperature, volatile-rich oxide melts (Nyström and Henríquez 1994; Frietsch and Perdahl 1995; Henríquez and Nyström 1998; Naslund et al. 2002; Henríquez et al. 2003; Velasco et al. 2016).

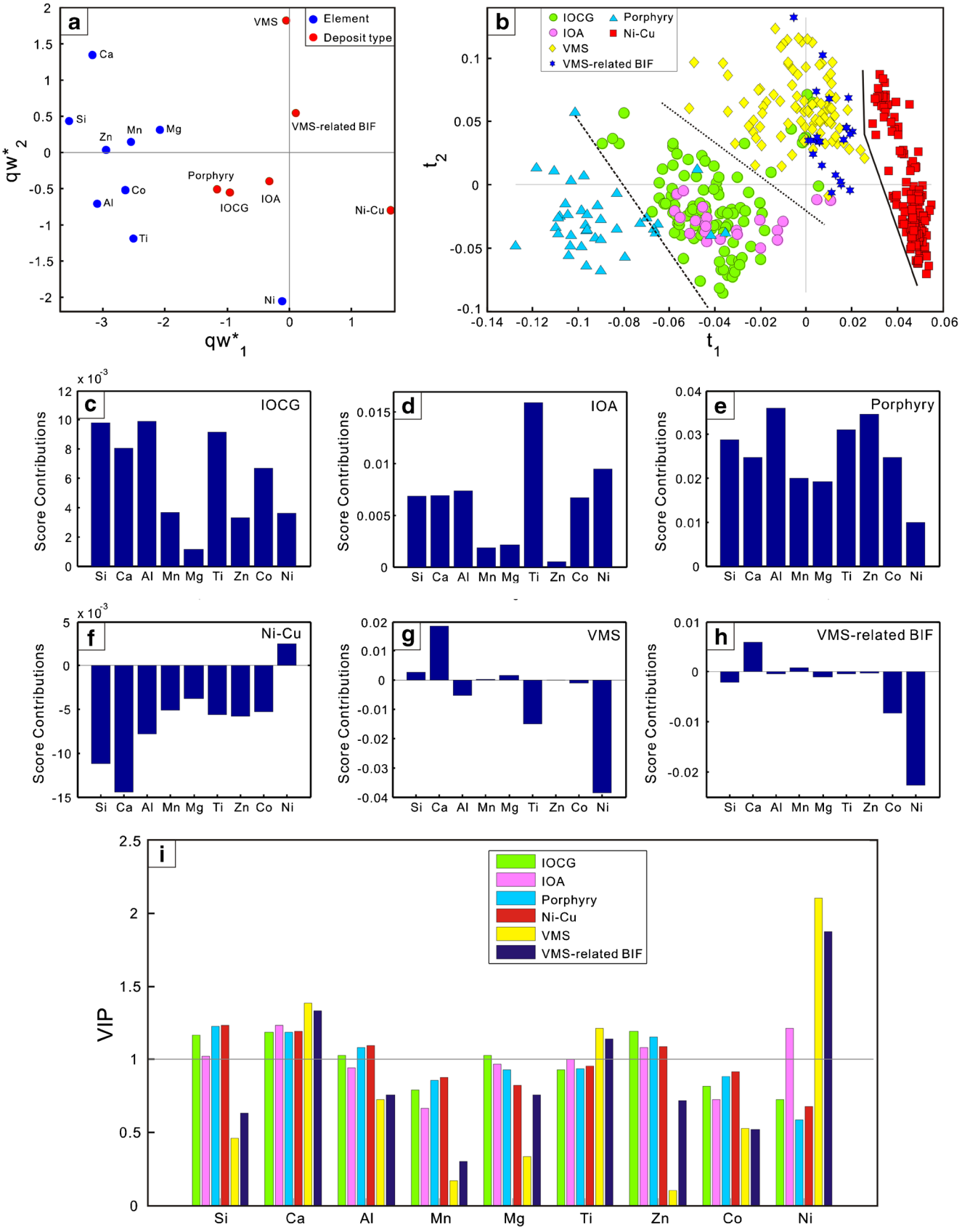
a
Element
Deposit type
VMS
Ca
Si
Mn
Mg
Zn
VMS-related BIF
Porphyry
Co
IOA
Al
IOCG
Ni-Cu
Ti
Ni
qw*2
qw*1
b
IOCG
Porphyry
IOA
Ni-Cu
VMS
VMS-related BIF
t2
t1
c
IOCG
d
IOA
e
Porphyry
f
Ni-Cu
g
VMS
h
VMS-related BIF
Score Contributions
x 10-3
Si Ca Al Mn Mg Ti Zn Co Ni
i
IOCG
IOA
Porphyry
Ni-Cu
VMS
VMS-related BIF
VIP

◀ **Fig. 11** PLS-DA results of chemical composition of iron oxides from different types of deposits. **a** Plot of qw^*_1 vs. qw^*_2 (first and second loadings) showing correlations among element variables and deposit types. **b** Plot of t_1 vs. t_2 (first and second scores) showing the distribution of individual analyses from different deposit types in the latent variable space defined by qw^*_1–qw^*_2 in (**a**). **c**–**h** Score contribution plots of elements for different deposit types. **i** The VIP showing the importance of compositional variables in classification of samples in (**b**). Data sources: IOCG and IOA deposits (this study), porphyry deposits (unpublished data of Huang et al.), Ni–Cu sulfide deposits (Boutroy et al. 2014), VMS deposits and VMS-related BIF (Makvandi et al. 2016a, b)

Knipping et al. (2015a, b) proposed a model for IOA formation by flotation of magmatic magnetite suspensions explaining the change from purely magmatic to magmatic–hydrothermal magnetite at Los Colorados (Chile), in which IOA deposits are interpreted to represent the deeper roots of an Andean IOCG system (Sillitoe 2003). This model is also supported by trace element geochemistry of pyrite from the same deposit (Reich et al. 2016). If some authors conclude that currently available data are inadequate to argue for or against a direct process link between IOA and IOCG deposits (Williams 2010b), others have been able to map the transition from IOA to IOCG mineralization and their associated alteration facies (Mumin et al. 2010; Corriveau et al. 2016; Montreuil et al. 2016; Ehrig et al. 2017). In this section, we compare trace element compositions of iron oxides between IOCG and IOA deposits and investigate the possible relationship between them.

Magnetite-group IOCG deposits overlap to some extent with magnetite and magnetite + hematite IOA deposits in the t_1–t_2 space defined by EPMA data (Fig. 9b), due to the similar chemistry of their iron oxides in terms of Si, Al, Mg, Mn, Ca, V, and Ti. A compositional overlap between IOCG and IOA deposits also exist for the limited number of chemical variables from EPMA data (Fig. 8b). In contrast, the larger number of trace elements measured by LA-ICP-MS allows discriminating IOCG from IOA deposits (Fig. 8c, d). For example, samples from IOCG deposits are characterized by higher Si, Al, Ge, Nb, Cu, Mo, Ga, and Zn contents, whereas those from IOA deposits show higher Mg, Ti, V, Pb, and Sc contents (Fig. 8c, d). The higher Ti and V contents in iron oxides from IOA compared to IOCG deposits are important discrimination factors for these two types of deposits (Dupuis and Beaudoin 2011). Because Ti + V content in magnetite is a function of temperature and oxygen fugacity (Nadoll et al. 2014, 2015), the higher Ti + V content in iron oxides from IOA deposits is likely to reflect higher formation temperature and oxygen fugacity. The similar alteration types (e.g., Ca–Fe alteration) and overlapping magnetite chemistry between IOCG and IOA deposits (Figs. 8b, 9b, d, and 11b) are permissive evidence for a genetic link between IOCG and IOA deposits despite formation under different temperatures and oxygen fugacity conditions. Whether IOCG and IOA deposits formed at different stages of a common magmatic or magmatic–hydrothermal system, or that they formed separately, remains unresolved based on iron oxide chemistry.

Comparison of IOCG and IOA iron oxide composition with other deposit types

Makvandi et al. (2016b) showed that PLS-DA is a robust classification method to distinguish the chemical composition of magnetite from different VMS settings, as well as different types of mineral deposits. Iron oxides from IOCG and IOA deposits overlap together in the t_1–t_2 plot (Fig. 11a, b), consistent with lack of discrimination using trace elements measured by EPMA (Fig. 8a, b). IOCG and IOA deposits are separated from porphyry, VMS, VMS-related BIF, and Ni–Cu sulfide deposits using their iron oxide chemistry (Fig. 11b–d). Iron oxides from porphyry Cu deposits plot at low t_1 values relative to IOCG deposits and IOA deposits (Fig. 11b), as a result of covariation of Si, Ca, Al, Co, and Ti (Fig. 11e). Ni–Cu sulfide deposits can be discriminated from other types of deposits due to positive t_2 from correlated Ni and inversely correlated Si, Ca, Al, Mn, Mg, Ti, Zn, and Co in magnetite (Fig. 11f). This is consistent with the results of Dupuis and Beaudoin (2011) that iron oxides from Ni–Cu sulfide deposits are relatively rich in Ni and Cr but depleted in Si and Mg, and thus explaining why the Ni + Cr versus Si + Mg diagram is useful to discriminate Ni–Cu sulfide deposits from other types of deposits (Boutroy et al. 2014). Iron oxides from VMS deposits and VMS-related BIF are separated from those from other types of deposits by t_2 due to correlated Ca but inversely correlated Ni (Fig. 11g, h), consistent with the results of Makvandi et al. (2016b). The VIP plot indicates that Si and Zn are important discriminator elements for all the selected deposit types but VMS and VMS-related BIF (Fig. 11i). The relative depletion of Si and Zn in VMS and VMS-related BIF is possibly due to the strong partitioning of Si in quartz and Zn in sphalerite, co-precipitated with magnetite. Calcium is an important discriminating element for all deposit types (Fig. 11i). Aluminum is important in discriminating IOCG, porphyry, and Ni–Cu sulfide deposits, perhaps because these deposits are magma-related (Fig. 11i). Titanium is important to discriminate VMS, VMS-related BIF, and IOA deposits (Fig. 11i). Nickel is the important discriminant element for IOA, VMS deposits, and VMS-related BIF (Fig. 11i). IOA deposits are Fe-sulfide deficient compared to VMS system, such that Ni partitions in magnetite. The relative depletion of Ni in magnetite from VMS deposits and VMS-related BIF is possibly due to partitioning of Ni into pyrrhotite co-precipitating with magnetite (Makvandi et al. 2016a).

Conclusions

The trace element composition of iron oxides from IOCG and IOA deposits is controlled by oxygen fugacity, temperature, co-precipitating minerals (mainly Fe-sulfides), and host rocks particularly granitic. The iron oxide chemistry is not related to the iron oxide mineralogy (magnetite vs. hematite) in the same deposit but closely related to alteration and deposit types. The trace element composition of iron oxides can thus serve as a proxy for hydrothermal alteration and deposit types. Iron oxides from high-temperature Ca–Fe alteration can be separated from those from high- and low-temperature K–Fe alteration by higher Mg and V contents, whereas iron oxides from low-temperature K–Fe alteration can be discriminated from high-temperature K–Fe alteration by higher W, Sn, Nb, Mo, and Zr contents. The iron oxide compositions of hematite IOCG, magnetite IOA, and magnetite + hematite IOA deposits can be classified, whereas magnetite IOCG deposits overlap with the three other deposit subtypes. The compositional diversity of iron oxides from magnetite IOCG deposits may be due to the incremental development of high-temperature Ca–Fe and K–Fe alteration associated with these deposits. The overlapping chemical composition of iron oxides from IOCG and IOA deposits are permissive evidence for a genetic link between them despite formation under different temperatures and oxygen fugacity conditions.

Acknowledgements This project was funded by China Scholarship Council (CSC, 201604910462), the Natural Science and Engineering Research Council (NSERC) of Canada, Agnico Eagle Mines Limited, and Ministry of Natural Resources of Quebec within the NSERC–Agnico Eagle Industrial Research Chair in Mineral Exploration. It is also conducted in collaboration with participants of the Targeted Geoscience Initiative program of the Geological Survey of Canada (GSC). We thank Marc Choquette (Laval U.) and Dany Savard (UQAC) for their assistance with EPMA and LA-ICP-MS analyses, respectively. Special thanks to Michel Jebrak (UQAM), Sarah Dare (U. of Ottawa), Lluis Fontboté (U. of Geneva), Isabelle McMartin (GSC), Roberto Perez Xavier (USP São Paulo), Robert Marschik (LMU Munich), and John Hanchar (Memorial U. of Newfoundland) who provided representative samples. We thank Pedro Acosta-Góngora (GSC) for constructive comments on the early manuscript. We also acknowledge careful reviews by Jaayke Knipping and an anonymous reviewer, and editorial handling by Frank Melcher and Bernd Lehmann.

References

Acosta-Góngora P, Gleeson S, Samson I, Ootes L, Corriveau L (2014) Trace element geochemistry of magnetite and its relationship to Cu-Bi-Co-Au-Ag-UW mineralization in the Great Bear magmatic zone, NWT, Canada. Econ Geol 109:1901–1928

Aitchison J (1986) The statistical analysis of compositional data. Chapman and Hall Ltd., London, UK, pp 1–416

Angerer T, Hagemann SG, Danyushevsky LV (2012) Geochemical evolution of the banded iron formation-hosted high-grade iron ore system in the Koolyanobbing Greenstone Belt, Western Australia. Econ Geol 107:599–644

Apukhtina OB, Kamenetsky VS, Ehrig K, Kamenetsky MB, Maas R, Thompson J, McPhie J, Ciobanu CL, Cook NJ (2017) Early, deep magnetite–fluorapatite mineralization at the Olympic dam Cu-U-Au-Ag deposit, South Australia. Econ Geol 112:1531–1542

Barnes SJ, Roeder PL (2001) The range of spinel compositions in terrestrial mafic and ultramafic rocks. J Petrol 42:2279–2302

Barreira CF, Soares ADV, Ronzê PC (1999) Descoberta do depósito Cu–Au Alemão—Província Mineral de Carajás (PA). In: SBG, 6° Simpósio de Geologia da Amazônia, Manaus, AM, vol 6. Bol Res Expandidos, pp 136–139

Barton MD, Johnson DA (1996) Evaporitic-source model for igneous-related Fe oxide–(REE-Cu-Au-U) mineralization. Geology 24:259–262

Bastrakov EN, Skirrow RG, Davidson GJ (2007) Fluid evolution and origins of iron oxide Cu-Au prospects in the Olympic Dam district, Gawler craton, South Australia. Econ Geol 102:1415–1440

Beaudoin G, Dupuis C (2010) Iron-oxide trace element fingerprinting of mineral deposit types. In: Corriveau L, Mumin AH (eds) Exploring for iron oxide copper–gold deposits: Canada and global analogues. Geological Association of Canada, Short Course Notes, vol 20, pp 107–121

Bookstrom AA (1977) The magnetite deposits of El Romeral, Chile. Econ Geol 72:1101–1130

Boutroy E, Dare SAS, Beaudoin G, Barnes S-J, Lightfoot PC (2014) Magnetite composition in Ni-Cu-PGE deposits worldwide and its application to mineral exploration. J Geochem Explor 145:64–81

Brereton RG, Lloyd GR (2014) Partial least squares discriminant analysis: taking the magic away. J Chemom 28:213–225

Broughm SG, Hanchar JM, Tornos F, Westhues A, Attersley S (2017) Mineral chemistry of magnetite from magnetite-apatite mineralization and their host rocks: examples from Kiruna, Sweden, and El Laco, Chile. Miner Deposita 52:1223–1244

Buddington A, Lindsley D (1964) Iron-titanium oxide minerals and synthetic equivalents. J Petrol 5:310–357

Carew MJ (2004) Controls on Cu-Au mineralisation and Fe oxide metasomatism in the Eastern Fold Belt, NW Queensland, Australia. Ph.D. thesis, James Cook University, Queensland, pp 213–277

Carlon CJ (2000) Iron oxide systems and base metal mineralisation in northern Sweden. In: Porter TM (ed) Hydrothermal iron oxide copper–gold and related deposits: a global perspective, vol 1. PGC Publishing, Adelaide, pp 283–296

Chen WT, Zhou M-F, Gao J-F, Hu RZ (2015) Geochemistry of magnetite from Proterozoic Fe-Cu deposits in the Kangdian metallogenic province, SW China. Miner Deposita 50:795–809

Clark T, Gobeil A, Chevé S (2010) Alterations in IOCG-type and related deposits in the Manitou Lake area, eastern Grenville Province, Québec. In: Corriveau L, Mumin H (eds) Exploring for iron oxide copper-gold deposits: Canada and global analogues. Geological Association of Canada, Short Course Notes, vol 20, pp 127–146

Clark T, Gobeil A, David J (2005) Iron oxide-copper-gold-type and related deposits in the Manitou Lake area, eastern Grenville Province, Quebec: variations in setting, composition, and style. Can J Earth Sci 42:1829–1847

Cornell RM, Schwertmann U (2003) The iron oxides: structure, properties, reactions, occurrences and uses. John Wiley & Sons, Weinheim, pp 1–694

Corriveau L, Ootes L, Mumin H, Jackson V, Bennett V, Cremer JF, Rivard B, McMartin I, Beaudoin G (2007) Alteration vectoring to IOCG(U) deposits in frontier volcano-plutonic terrains, Canada. In: Milkereit B (ed) Proceedings of exploration 07: fifth decennial international conference on mineral exploration, pp 1171–1177

Corriveau L, Williams PJ, Mumin AH (2010) Alteration vectors to IOCG mineralization—from uncharted terranes to deposits. In: Corriveau L, Mumin H (eds) Exploring for iron oxide copper–gold deposits: Canada and global analogues. Geological Association of Canada, Short Course Notes, vol 20, pp 89–110

Corriveau L, Montreuil J-F, Potter E (2016) Alteration facies linkages among iron oxide copper–gold, iron oxide–apatite, and affiliated deposits in the Great Bear magmatic zone, northwest territories, Canada. Econ Geol 111:2045–2072

Corriveau L, Potter EG, Acosta-Gongora P, Blein O, Montreuil J-F, De Toni AF, Day W, Slack JF, Ayuso RA, Hanes R (2017) Petrological mapping and chemical discrimination of alteration facies as vectors to IOA, IOCG, and affiliated deposits within Laurentia and beyond. Proceedings of the 14th SGA Biennial Meeting, 20–23 August 2017, Québec City, pp 851–855

Cygan GL, Candela PA (1995) Preliminary study of gold partitioning among pyrrhotite, pyrite, magnetite, and chalcopyrite in gold-saturated chloride solutions at 600 to 700°C, 140 MPa, 1400 bars. In: Thompson JFH (ed) Magmas, fluids, and ore deposits, vol 23. Mineralogical Association of Canada Short Course, pp 129–137

Dare SAS, Barnes S-J, Beaudoin G (2012) Variation in trace element content of magnetite crystallized from a fractionating sulfide liquid, Sudbury, Canada: implications for provenance discrimination. Geochim Cosmochim Acta 88:27–50

Dare SAS, Barnes S-J, Beaudoin G, Méric J, Boutroy E, Potvin-Doucet C (2014) Trace elements in magnetite as petrogenetic indicators. Miner Deposita 49:785–796

Day WC, Slack JF, Ayuso RA, Seeger CM (2016) Regional geologic and petrologic framework for iron oxide ± apatite ± rare earth element and iron oxide copper–gold deposits of the Mesoproterozoic St. Francois mountains terrane, Southeast Missouri, USA. Econ Geol 111:1825–1858

Deditius AP, Reich M, Simon AC, Suvorova A, Knipping J, Roberts MP, Rubanov S, Dodd A, Saunders M (2018) Nanogeochemistry of hydrothermal magnetite. Contrib Mineral Petrol 173:46

De Iorio M, Ebbels TMD, Stephens DA (2008) Statistical techniques in metabolic profiling. In: Handbook of statistical genetics. John Wiley & Sons, Ltd, pp 347–373

De Toni AF (2016) Les paragenèses à magnétite des altérations associées aux systèmes à oxydes de fer et altérations en éléments alcalins, zone magmatique du Grand lac de l'Ours. MSc thesis, Université du Québec, Institut National de la Recherche Scientifique-Centre Eau Terre Environnement, pp 1–549

Dreher AM, Xavier RP, Taylor BE, Martini SL (2008) New geologic, fluid inclusion and stable isotope studies on the controversial Igarapé Bahia Cu–Au deposit, Carajás Province, Brazil. Miner Deposita 43:161–184

Dupuis C, Beaudoin G (2011) Discriminant diagrams for iron oxide trace element fingerprinting of mineral deposit types. Miner Deposita 46: 1–17

Egozcue JJ, Pawlowsky-Glahn V, Mateu-Figueras G, Barcelo-Vidal C (2003) Isometric logratio transformations for compositional data analysis. Math Geol 35:279–300

Ehrig K, Kamenetsky VS, McPhie J, Apukhtina O, Ciabanu CL, Cook N, Kontonikas-Charos A, Krneta S (2017) The IOCG-IOA Olympic Dam Cu-U-Au-Ag deposit and nearby prospects, South Australia. Proceedings of the 14th SGA Biennial Meeting, 20–23 August 2017, Québec City, pp 823–827

Ehrig K, McPhie J, Kamenetsky V (2012) Geology and mineralogical zonation of the Olympic Dam iron oxide Cu–U–Au–Ag deposit, South Australia. In: Hedenquist JW, Harris M, Camus F (eds) Geology and genesis of major copper deposits of the world. Society of Economic Geologists, special publication 16, Littleton, pp 237–267

Einaudi MT, Meinert LD, Newberry RJ (1981) Skarn deposits. Econ Geol 75:317–391

Eriksson L, Byrne T, Johansson E, Trygg J, Vikström C (2013) Multi- and megavariate data analysis: basic principles and applications. MKS Umetrics AB, Sweden, pp 1–521

Fleet ME (1981) The structure of magnetite. Acta Cryst B 37:917–920

Fleet ME, Crocket JH, Stone WE (1996) Partitioning of platinum-group elements (Os, Ir, Ru, Pt, Pd) and gold between sulfide liquid and basalt melt. Geochim Cosmochim Acta 60:2397–2412

Frietsch R, Perdahl J-A (1995) Rare earth elements in apatite and magnetite in Kiruna-type iron ores and some other iron ore types. Ore Geol Rev 9:489–510

Frost BR (1991) Stability of oxide minerals in metamorphic rocks. Rev Mineral Geochem 25:469–488

Frost BR, Lindsley DH (1991) Occurrence of iron-titanium oxides in igneous rocks. Rev Mineral Geochem 25:433–468

Gauthier M, Chartrand F, Cayer A, David J (2004) The Kwyjibo Cu-REE-U-Au-Mo-F property, Quebec: a mesoproterozoic polymetallic iron oxide deposit in the northeastern Grenville Province. Econ Geol 99:1177–1196

Geijer P (1910) Igneous rocks and iron ores of Kiirunavaara, Luossavaara and Tuolluvaara. Scientific and practical researches in Lapland arranged by Luossavaara-Kiirunavaara Aktiebolag. PhD thesis, University Uppsala, Uppsala, Sweden, pp 1–278

Ghiorso MS, Sack O (1991) Fe–Ti oxide geothermometry: thermodynamic formulation and the estimation of intensive variables in silicic magmas. Contrib Mineral Petrol 108:485–510

Goldschmidt VM (1958) Geochemistry. Oxford University Press, London, pp 1–730

Green GR (2012) Ore deposits and metallogenesis of Tasmania. Episodes 35:205–215

Grigsby JD (1990) Detrital magnetite as a provenance indicator. J Sediment Res 60:940–951

Heidarian H, Lentz D, Alirezaei S, Peighambari S, Hall D (2016) Using the chemical analysis of magnetite to constrain various stages in the formation and genesis of the Kiruna-type chadormalu magnetite–apatite deposit, Bafq district, Central Iran. Mineral Petrol 110:927–942

Helsel DR (2005) Nondetects and data analysis. Statistics for censored environmental data. Wiley-Interscience, New York, pp 1–268

Henríquez F, Naslund HR, Nyström JO, Vivallo W, Aguirre R, Dobbs FM, Lledó H (2003) New field evidence bearing on the origin of the El Laco magnetite deposit, northern Chile—a discussion. Econ Geol 98:1497–1500

Henríquez F, Nyström JO (1998) Magnetite bombs at El Laco volcano, Chile. GFF 120:269–271

Hitzman MW (2000) Iron oxide-Cu-Au deposits: what, where, when, and why. In: Porter TM (ed) Hydrothermal iron oxide copper-gold & related deposits: a global perspective, vol 1. PGC Publishing, Adelaide, pp 9–25

Hitzman MW, Oreskes N, Einaudi MT (1992) Geological characteristics and tectonic setting of Proterozoic iron oxide (Cu ± U ± Au ± REE) deposits. Precambrian Res 58:241–287

Hron K, Templ M, Filzmoser P (2010) Imputation of missing values for compositional data using classical and robust methods. Comput Stat Data Anal 54:3095–3107

Hu H, Lentz D, Li J-W, McCarron T, Zhao X-F, Hall D (2015) Reequilibration processes in magnetite from iron skarn deposits. Econ Geol 110:1–8

Huang X-W, Zhou M-F, Qi L, Gao J-F, Wang Y-W (2013) Re–Os isotopic ages of pyrite and chemical composition of magnetite from the Cihai magmatic–hydrothermal Fe deposit, NW China. Miner Deposita 48: 925–946

Huang X-W, Qi L, Meng Y-M (2014) Trace element geochemistry of magnetite from the Fe(-Cu) deposits in the Hami region, eastern Tianshan Orogenic Belt, NW China. Acta Geol Sin 88:176–195

Huang X-W, Gao J-F, Qi L, Zhou M-F (2015a) In-situ LA-ICP-MS trace elemental analyses of magnetite and Re–Os dating of pyrite: the Tianhu hydrothermally remobilized sedimentary Fe deposit. NW China Ore Geol Rev 65:900–916

Huang X-W, Zhou M-F, Qiu Y-Z, Qi L (2015b) In-situ LA-ICP-MS trace elemental analyses of magnetite: the Bayan Obo Fe–REE–Nb deposit. North China Ore Geol Rev 65:884–899

Huang X-W, Gao J-F, Qi L, Meng Y-M, Wang Y-C, Dai Z-H (2016) In-situ LA-ICP-MS trace elements analysis of magnetite: the Fenghuangshan Cu-Fe-Au deposit, Tongling, Eastern China. Ore Geol Rev 72:746–759

Huang X-W, Zhou M-F, Beaudoin G, Gao J-F, Qi L, Lyu C (2018) Origin of the volcanic-hosted Yamansu Fe deposit, eastern Tianshan, NW China: constraints from pyrite Re-Os isotopes, stable isotopes, and in situ magnetite trace elements. Miner Deposita. https://doi.org/10.1007/s00126-018-0794-4

Huberty JM, Konishi H, Heck PR, Fournelle JH, Valley JW, Xu H (2012) Silician magnetite from the Dales Gorge member of the Brockman Iron Formation, Hamersley group, Western Australia. Am Mineral 97:26–37

Ilton ES, Eugster HP (1989) Base metal exchange between magnetite and a chloride-rich hydrothermal fluid. Geochim Cosmochim Acta 53:291–301

Jarosewich E, Nelen J, Norberg JA (1980) Reference samples for electron microprobe analysis. Geostand Newslett 4:43–47

Knipping JL, Bilenker LD, Simon AC, Reich M, Barra F, Deditius AP, Lundstrom C, Bindeman I, Munizaga R (2015a) Giant Kiruna-type deposits form by efficient flotation of magmatic magnetite suspensions. Geology 43:591–594

Knipping JL, Bilenker LD, Simon AC, Reich M, Barra F, Deditius AP, W lle M, Heinrich CA, Holtz F, Munizaga R (2015b) Trace elements in magnetite from massive iron oxide-apatite deposits indicate a combined formation by igneous and magmatic-hydrothermal processes. Geochim Cosmochim Acta 171:15–38

Kontonikas-Charos A, Ciobanu CL, Cook NJ, Ehrig K, Krneta S, Kamenetsky VS (2017) Feldspar evolution in the Roxby Downs granite, host to Fe-oxide Cu-Au-(U) mineralisation at Olympic Dam, South Australia. Ore Geol Rev 80:838–859

Lee L, Helsel D (2007) Statistical analysis of water-quality data containing multiple detection limits II: S-language software for nonparametric distribution modeling and hypothesis testing. Comput Geosci 33:696–704

Lindenmayer ZG, Teixeira JBG (1999) Ore genesis at the Salobo copper deposit, Serra dos Carajás. In: Silva MG, Misi A (eds) Base metal deposits of Brazil. MME/CPRM/DNPM, pp 33–43

Lindsley DH (1976) The crystal chemistry and structure of oxide minerals as exemplified by the Fe-Ti oxides. In: Rumble IIID (ed) Oxide Minerals. Rev Mineral, pp L1–L60

Liu P-P, Zhou M-F, Chen WT, Gao J-F, Huang X-W (2015) In-situ LA-ICP-MS trace elemental analyses of magnetite: Fe–Ti–(V) oxide-bearing mafic–ultramafic layered intrusions of the Emeishan Large Igneous Province. SW China Ore Geol Rev 65:853–871

Loberg BEH, Horndahl AK (1983) Ferride geochemistry of Swedish Precambrian iron ores. Miner Deposita 18:487–504

Makvandi S, Beaudoin G, McClenaghan BM, Layton-Matthews D (2015) The surface texture and morphology of magnetite from the Izok Lake volcanogenic massive sulfide deposit and local glacial sediments, Nunavut, Canada: application to mineral exploration. J Geochem Explor 150:84–103

Makvandi S, Ghasemzadeh-Barvarz M, Beaudoin G, Grunsky EC, McClenaghan MB, Duchesne C (2016a) Principal component analysis of magnetite composition from volcanogenic massive sulfide deposits: case studies from the Izok Lake (Nunavut, Canada) and Halfmile Lake (New Brunswick, Canada) deposits. Ore Geol Rev 72:60–85

Makvandi S, Ghasemzadeh-Barvarz M, Beaudoin G, Grunsky EC, McClenaghan MB, Duchesne C, Boutroy E (2016b) Partial least squares-discriminant analysis of trace element compositions of magnetite from various VMS deposit subtypes: application to mineral exploration. Ore Geol Rev 78:388–408

Mark G, Oliver NH, Williams PJ (2006) Mineralogical and chemical evolution of the Ernest Henry Fe oxide–Cu–Au ore system, Cloncurry district, Northwest Queensland, Australia. Miner Deposita 40:769–801

Marschik R, Fontboté L (2001) The Candelaria-Punta del Cobre iron oxide Cu-Au (-Zn-Ag) deposits, Chile. Econ Geol 96:1799–1826

Marschik R, Chiaradia M, Fontboté L (2003) Implications of Pb isotope signatures of rocks and iron oxide Cu-Au ores in the Candelaria-Punta del Cobre district, Chile. Mineral Deposita 38:900–912

Martinsson O, Billström K, Broman C, Weihed P, Wanhainen C (2016) Metallogeny of the northern Norrbotten Ore Province, northern Fennoscandian shield with emphasis on IOCG and apatite-iron ore deposits. Ore Geol Rev 78:447–492

Matthews A (1976) Magnetite formation by the reduction of hematite with iron under hydrothermal conditions. Am Mineral 6:927–932

McLelland J, Morrison J, Selleck B, Cunningham B, Olson C, Schmidt K (2002) Hydrothermal alteration of late- to post-tectonic Lyon Mountain granitic gneiss, Adirondack Mountains, New York: origin of quartz–sillimanite segregations, quartz–albite lithologies, and associated Kiruna-type low-Ti Fe-oxide deposits. J Metamorph Geol 20:175–190

Meinert LD, Dipple GM, Nicolescu S (2005) World skarn deposits. In: Hedenquist JW, Thompson JFH, Goldfarb RJ, Richards JP (eds) Economic geology 100th anniversary volume. Society of Economic Geologists. Littleton, Colorado, pp 299–336

Monteiro LVS, Xavier RP, De Carvalho ER, Hitzman MW, Johnson CA, De Souza Filho CR, Torresi I (2008a) Spatial and temporal zoning of hydrothermal alteration and mineralization in the Sossego iron oxide–copper–gold deposit, Carajás Mineral Province, Brazil: paragenesis and stable isotope constraints. Miner Deposita 43:129–159

Monteiro LVS, Xavier RP, Hitzman MW, Juliani C, De Souza Filho CR, Carvalho ER (2008b) Mineral chemistry of ore and hydrothermal alteration at the Sossego iron oxide–copper–gold deposit, Carajás Mineral Province, Brazil. Ore Geol Rev 34:317–336

Montreuil JF, Corriveau L, Grunsky EC (2013) Compositional data analysis of hydrothermal alteration in IOCG systems, Great Bear magmatic zone, Canada: to each alteration type its own geochemical signature. Geochem Explor Environ Anal 13:229–247

Montreuil J-F, Corriveau L, Potter E, De Toni A (2016) On the relationship between alteration facies and metal endowment of iron oxide-alkali-altered systems, southern Great Bear magmatic zone (Canada). Econ Geol 111:2139–2168

Müller B, Axelsson MD, Öhlander B (2003) Trace elements in magnetite from Kiruna, northern Sweden, as determined by LA-ICP-MS. GFF 125:1–5

Mumin AH, Somarin AK, Jones B, Corriveau L, Ootes L, Camier J (2010) The IOCG-porphyry-epithermal continuum in the Great Bear magmatic zone, northwest territories, Canada. In: Corriveau L, Mumin AH (eds) Exploring for iron-oxide copper-gold deposits: Canada and global analogues. Geological Association of Canada, Short Course Notes, vol 20, pp 59–78

Nadoll P, Angerer T, Mauk JL, French D, Walshe J (2014) The chemistry of hydrothermal magnetite: a review. Ore Geol Rev 61:1–32

Nadoll P, Mauk JL, Hayes TS, Koenig AE, Box SE (2012) Geochemistry of magnetite from hydrothermal ore deposits and host rocks of the Mesoproterozoic Belt Supergroup, United States. Econ Geol 107:1275–1292

Nadoll P, Mauk JL, Leveille RA, Koenig AE (2015) Geochemistry of magnetite from porphyry Cu and skarn deposits in the southwestern United States. Miner Deposita 50:493–515

Naslund HR, Henríquez F, Nyström JO, Vivallo W, Dobbs FM (2002) Magmatic iron ores and associated mineralization: examples from the Chilean high Andes and coastal Cordillera. In: Porter TM (ed) Hydrothermal iron oxide copper-gold and related deposits: a global perspective, vol 2. PGC Publishing, Adelaide, pp 207–226

Nold JL, Davidson P, Dudley MA (2013) The pilot knob magnetite deposit in the Proterozoic St. Francois mountains terrane, Southeast Missouri, USA: a magmatic and hydrothermal replacement iron deposit. Ore Geol Rev 53:446–469

Nuelle LM, Day WC, Sidder GB, Seeger CM (1992) Geology and mineral paragenesis of the Pea Ridge iron ore mine, Washington County, Missouri—origin of the rare-earth-element- and gold-bearing breccia pipes (United States Geological Survey Bulletin 1989). In: Day WC, Lane DE (eds) Strategic and critical minerals in the midcontinent region, United States, Chapter A. United States Government Printing Office, Washington, pp A1–A11

Nyström JO, Henríquez F (1994) Magmatic features of iron ores of the Kiruna type in Chile and Sweden; ore textures and magnetite geochemistry. Econ Geol 89:820–839

Ohmoto H (2003) Nonredox transformations of magnetite–hematite in hydrothermal systems. Econ Geol 98:157–161

Otake T, Wesolowski DJ, Anovitz LM, Allard LF, Ohmoto H (2010) Mechanisms of iron oxide transformations in hydrothermal systems. Geochim Cosmochim Acta 74:6141–6156

Putnis A, Austrheim H (2013) Mechanisms of metasomatism and metamorphism on the local mineral scale: the role of dissolution–reprecipitation during mineral re-equilibration. In: Harlov DE, Austrheim H (eds) Metasomatism and the chemical transformation of rock: the role of fluids in terrestrial and extraterrestrial processes. Springer-Verlag, Berlin-Heidelberg, pp 141–170

Ramdohr P (1980) The ore minerals and their intergrowths. Pergamon, New York, pp 1–1207

Razjigaeva N, Naumova V (1992) Trace element composition of detrital magnetite from coastal sediments of northwestern Japan Sea for provenance study. J Sediment Res 62:802–809

Reich M, Simon AC, Deditius A, Barra F, Chryssoulis S, Lagas G, Tardani D, Knipping J, Bilenker L, Sánchez-Alfaro P (2016) Trace element signature of pyrite from the Los Colorados iron oxide–apatite (IOA) deposit, Chile: a missing link between Andean IOA and iron oxide copper–gold systems? Econ Geol 111:743–761

Requia K, Fontboté L (2000) The Salobo iron oxide copper–gold deposit, Carajás, northern Brazil. In: Porter TM (ed) Hydrothermal iron-oxide copper–gold and related deposits: a global perspective, vol 1. PGC Publishing, Adelaide, pp 225–236

Requia K, Stein H, Fontboté L, Chiaradia M (2003) Re–Os and Pb–Pb geochronology of the Archean Salobo iron oxide copper–gold deposit, Carajás mineral province, northern Brazil. Miner Deposita 38: 727–738

Rhodes AL, Oreskes N, Sheets SA (1999) Geology and rare earth element (REE) geochemistry of magnetite deposits at El Laco, Chile. In: Skinner BJ (ed) Geology and ore deposits of the Central Andes. Soc Econ Geol Spec Publ, vol 7, pp 299–332

Righter K, Sutton SR, Newville M, Le L, Schwandt CS, Uchida H, Lavina B, Downs RT (2006) An experimental study of the oxidation state of vanadium in spinel and basaltic melt with implications for the origin of planetary basalt. Am Mineral 91:1643–1656

Ronzê PC, Soares ADV, dos Santos MGS, Barreira CF (2000) Alemão copper–gold (U-REE) deposit, Carajás, Brazil. In: Poter TM (ed) Hydrothermal iron oxide copper–gold & related deposits: a global perspective, vol 1. PGC Publishing, Adelaide, pp 191–202

Rudnick RL, Gao S (2003) Composition of the continental crust. In: Holland HD, Turekian KK (eds) Treatise on geochemistry, vol 3. The crust. Elsevier-Pergamon, Oxford, pp 1–64

Rusk B, Oliver N, Cleverley J, Blenkinsop T, Zhang D, Williams P, Habermann P (2010) Physical and chemical characteristics of the Ernest Henry iron oxide copper gold deposit, Australia; implications for IOCG genesis. In: Porter TM (ed) Hydrothermal iron oxide copper-gold & related deposits: a global perspective, vol 3. PGC Publishing, Adelaide, pp 1–18

Rusk BG, Oliver NHS, Zhang D, Brown A, Lilly R, Jungmann D (2009) Compositions of magnetite and sulfides from barren and mineralized IOCG deposits in the eastern succession of the Mt Isa Inlier, Australia. In: Proceedings of GSA Annual Meeting, 18–21 October 2009, Portland. Geol Soc Am Abstr Programs 41:84

Sappin A-A, Dupuis C, Beaudoin G, Pozza M, McMartin I, McClenaghan M (2014) Optimal ferromagnetic fraction in till samples along ice-flow paths: case studies from the Sue-Dianne and Thompson deposits, Canada. Geochem Explor Environ Anal 14: 315–329

Savard D, Barnes SJ, Dare S, Beaudoin G (2012) Improved calibration technique for magnetite analysis by LA-ICP-MS. Mineral Mag 76: 2329

Sidhu PS, Gilkes RJ, Posner AM (1981) Oxidation and ejection of nickel and zinc from natural and synthetic magnetites. Soil Sci Soc Am J 45:641–644

Sievwright RH, Wilkinson JJ, O'Neill HSC, Berry AJ (2017) Thermodynamic controls on element partitioning between titanomagnetite and andesitic–dacitic silicate melts. Contrib Mineral Petrol 172:62

Sillitoe RH (2003) Iron oxide–copper–gold deposits: an Andean view. Miner Deposita 38:787–812

Sillitoe RH, Burrows DR (2002) New field evidence bearing on the origin of the El Laco magnetite deposit, northern Chile. Econ Geol 97: 1101–1109

Simon AC, Candela PA, Piccoli PM, Mengason M, Englander L (2008) The effect of crystal-melt partitioning on the budgets of Cu, Au, and Ag. Am Mineral 93:1437–1448

Singoyi B, Danyushevsky L, Davidson GJ, Large R, Zaw K Determination of trace elements in magnetites from hydrothermal deposits using the LA ICP-MS technique. In: SEG Keystone Conference, Denver, USA, 2006. CD-ROM

Skirrow R (2010) "Hematite-group" IOCG ± U ore systems: tectonic settings, hydrothermal characteristics, and Cu-Au and U mineralizing processes. In: Corriveau L, Mumin H (eds) Exploring for iron oxide copper–gold deposits: Canada and global analogues. Geological Association of Canada, Short Course Notes, vol 20, pp 39–58

Sossi PA, Prytulak J, O'Neill HSC (2018) Experimental calibration of vanadium partitioning and stable isotope fractionation between hydrous granitic melt and magnetite at 800°C and 0.5 GPa. Contrib Mineral Petrol 173:27

Swann P, Tighe N (1977) High voltage microscopy of the reduction of hematite to magnetite. Metall Trans B 8:479–487

Tallarico FH, Figueiredo BR, Groves DI, Kositcin N, McNaughton NJ, Fletcher IR, Rego JL (2005) Geology and SHRIMP U–Pb geochronology of the Igarapé Bahia deposit, Carajás copper–gold belt, Brazil: an archean (2.57 Ga) example of iron-oxide Cu-Au-(U-REE) mineralization. Econ Geol 100:7–28

Tazava E, De Oliveira CG (2000) The Igarapé Bahia Au-Cu-(REE-U) deposit, Carajás Mineral Province, northern Brazil. In: Poter TM (ed) Hydrothermal iron oxide copper–gold & related deposits: a global perspective, vol 1. PGC Publishing, Adelaide, pp 203–212

Thió-Henestrosa S, Martín-Fernández J (2005) Dealing with compositional data: the freeware CoDaPack. Math Geol 37:773–793

Toplis MJ, Corgne A (2002) An experimental study of element partitioning between magnetite, clinopyroxene and iron-bearing silicate liquids with particular emphasis on vanadium. Contrib Mineral Petrol 144:22–37

Tornos F (2011) Magnetite–apatite and IOCG deposits formed by magmatic–hydrothermal evolution of complex calcalkaline melts. In: Proceedings of 11th biennial SGA meeting, 26–29 September 2011, Antofagasta, Chile, pp 443–445

Tornos F, Velasco F, Hanchar JM (2016) Iron-rich melts, magmatic magnetite, and superheated hydrothermal systems: the El Laco deposit, Chile. Geology 44:427–430

Torresi I, Xavier RP, Bortholoto DF, Monteiro LV (2012) Hydrothermal alteration, fluid inclusions and stable isotope systematics of the Alvo

118 iron oxide–copper–gold deposit, Carajás Mineral Province (Brazil): implications for ore genesis. Miner Deposita 47:299–323

Valley PM, Fisher CM, Hanchar JM, Lam R, Tubrett M (2010) Hafnium isotopes in zircon: a tracer of fluid–rock interaction during magnetite–apatite ("Kiruna-type") mineralization. Chem Geol 275:208–220

Velasco F, Tornos F, Hanchar JM (2016) Immiscible iron- and silica-rich melts and magnetite geochemistry at the El Laco volcano (northern Chile): evidence for a magmatic origin for the magnetite deposits. Ore Geol Rev 79:346–366

Wechsler BA, Lindsley DH, Prewitt CT (1984) Crystal structure and cation distribution in titanomagnetites ($Fe_{3-x}Ti_xO_4$). Am Mineral 69:754–770

Whalen JB, Chappell BW (1988) Opaque mineralogy and mafic mineral chemistry of I- and S-type granites of the Lachlan fold belt, southeast Australia. Am Mineral 73:281–296

Whitten EHT (1995) Open and closed compositional data in petrology. Math Geol 27:789–806

Williams PJ (2010a) Classifying IOCG deposits. In: Corriveau L, Mumin H (eds) Exploring for iron oxide copper–gold deposits: Canada and global analogues. Geological Association of Canada, Short Course Notes, vol 20, pp 13–22

Williams PJ (2010b) "Magnetite-group" IOCGs with special reference to Cloncurry (NW Queensland) and northern Sweden: settings, alteration, deposit characteristics, fluid sources, and their relationship to apatite-rich iron ores. In: Corriveau L, Mumin H (eds) Exploring for iron oxide copper–gold deposits: Canada and global analogues. Geological Association of Canada, Short Course Notes, vol 20, pp 23–38

Williams PJ, Barton MD, Johnson DA, Fontbote L, De Haller A, Mark G, Oliver NHS, Marschik R (2005) Iron oxide copper–gold deposits: geology, space–time distribution and possible modes of origin. In: Economic geology 100th anniversary volume. In: pp 371–405

Wold S, Sjöström M, Eriksson L (2001) PLS-regression: a basic tool of chemometrics. Chemom Intell Lab Syst 58:109–130

Xavier RP, Monteiro LVS, Moreto CPN, Pestilho ALS, De Melo GHC, Da Silva MAD, Aires B, Ribeiro C, E Silva FHF (2012) The iron oxide copper–gold systems of the Carajás mineral province, Brazil. Econ Geol Spec Publ 16:433–454

Xu H, Shen Z, Konishi H (2014) Si-magnetite nano-precipitates in silician magnetite from banded iron formation: Z-contrast imaging and ab initio study. Am Mineral 99:2196–2202

Zhang D, Rusk B, Oliver N, Dai T (2011) Trace element geochemistry of magnetite from the Ernest Henry IOCG Deposit, Australia. Proceedings of 11th Biennial SGA Meeting, 26–29 September 2011, Antofagasta, Chile, pp 479–481

Zhao WW, Zhou M-F (2015) In-situ LA–ICP-MS trace elemental analyses of magnetite: the Mesozoic Tengtie skarn Fe deposit in the Nanling range. South China Ore Geol Rev 65:872–883

Zhao X-F, Zhou M-F (2011) Fe–Cu deposits in the Kangdian region, SW China: a Proterozoic IOCG (iron-oxide–copper–gold) metallogenic province. Miner Deposita 46:731–747